Paramagnetic, Near-Infrared Fluorescent Mn-doped PbS Colloidal Nanocrystals

Andrew N. Knott, BSc (Hons).

Dissertation submitted to The University of Nottingham for the Degree of MSc by Research in Physics

September 2013

Abstract

This dissertation describes the effect that the controlled incorporation of manganese (Mn) has on the optical and magnetic properties of colloidal PbS nanoparticles.

Optical and temperature-dependent optical studies combined with structural and chemical characterisation indicate the formation of alloyed (PbMn)S nanoparticles with Mn-content up to approximately 8 %. The nanoparticle photoluminescence (PL) properties are strongly dependent on the Mn-content and the PL emission can be tuned by the Mn-content in the near-infrared (NIR) wavelength range (850-1200 nm). Magnetisation and electron paramagnetic resonance (EPR) measurements show that the incorporation of manganese imprints PbS nanoparticles with paramagnetic properties.

A study of a number of photoinduced phenomena is also presented. It is found that the continuous exposure of the nanoparticles to laser light leads to a blue-shift of the PL emission energy and an enhancement of the PL intensity. Raman spectroscopy is also used to further investigate these phenomena, which are attributed to a photo-oxidation of the nanoparticles surface.

The solubility of (PbMn)S nanoparticles and their duel functionality, i.e. NIR luminescence and paramagnetism, could open up exciting prospects for the future exploitation of these nanocrystals as imaging labels for combined fluorescence and magnetic resonance imaging (MRI).

List of Publications

1. Turyanska L., Moro F., Knott A., Fay M., Bradshaw T., Patané A. "Paramagnetic, Near-Infrared Fluorescent Mn-doped PbS Colloidal Nanocrystals", to be published in *Particle and Particle System Characterizations*, (2013).
   http://onlinelibrary.wiley.com/doi/10.1002/ppsc.201300184/pdf

2. Poster presentation: "Paramagnetic, Near-Infrared Fluorescent Mn-doped PbS Colloidal Nanocrystals", *16th International Conference on Modulated Semiconductor Structures, Wroclaw, Poland*, (2013).

Acknowledgements

First, I would like to express my gratitude to my supervisor, Professor Amalia Patané, for her academic support, supervision and inspiration during this year of study. The guidance of Dr. Lyudmila Turyanska's on the use of different experimental techniques, fabrication of samples, knowledge and advice have also been invaluable.

I would like take this opportunity to, again, give my deepest thanks to both Amalia and Lyudmila for their support, patience and encouragement in overcoming some personal health issues which have, at times, made this a difficult year.

My thanks go to Fabrizio Moro from the University of Manchester for his collaboration on the EPR experiments. I would also like to thank Michael Fay from the University of Nottingham for his assistance in the TEM experiments.

I acknowledge The University of Nottingham for supporting this research and The UK National EPR Facility and Service in the Photon Science Institute at The University of Manchester for the use of their facilities.

My special thanks to all my colleagues in the group for their friendship, advice, assistance with experiments and for helping to provide a fruitful and enjoyable year of my life.

I would also like to thank my family and friends for their personal support and encouragement throughout the year.

Contents

1 Introduction **1**

2 Background **4**

2.1 Properties of Bulk Lead Sulphide and Manganese Sulphide 4

2.1.1 Bulk Lead Sulphide 4

2.1.2 Manganese and Bulk Manganese Sulphide 6

2.2 Quantum Confinement 7

2.3 Mn-doped PbS Colloidal Quantum Dots 12

2.4 QDs as fluorescent biolabels and MRI contrast agents 17

3 Synthesis and Experimental Techniques **19**

3.1 Synthesis 19

3.2 Photoluminescence 20

3.2.1 PL Experimental Setup 22

3.3 Raman Spectroscopy 24

3.4 Magnetic Measurements 26

3.4.1 Electron Paramagnetic Resonance Spectroscopy 26

3.4.2 SQUID Measurements 28

3.5 Energy-Dispersive X-ray Spectroscopy 28

3.6 Atomic Force Microscopy 29

3.7 Transmission Electron Microscopy 31

4 Effects of Mn-doping on the Physical Properties of PbS Nanoparticles 32

4.1 Morphology of the Nanoparticles 32

4.2 PL Properties 36

4.3 Temperature Dependence of PL Properties 39

4.4 Magnetic Properties 45

5 Photoinduced Phenomena in $Pb_{1-x}Mn_xS$ Nanoparticles 47

5.1 Photoinduced changes in the PL properties 47

5.1.1 Blue-shift of the PL Peak Energy 47

5.1.2 Photoenhancement of the PL Intensity 52

5.1.3 Photoinduced Quenching of the Mn-related PL Emission . . 55

5.2 Photoinduced Raman Peaks 58

6 Conclusions and Prospects for Future Work **64**

References **67**

List of Figures

2.1 Band structure of bulk PbS. 5

2.2 First Brillouin zone of an fcc lattice. 6

2.3 DOS for a 3D system. 8

2.4 DOS for a quantum well. 8

2.5 DOS for a quantum wire. 9

2.6 DOS for a quantum dot. 9

2.7 Schematic diagram of the exciton and exciton energy levels. 10

2.8 Dependence of E_{QD} on nanocrystal diameter due to confinement effects for PbS nanoparticles. 12

2.9 Cartoon showing self-purification process for a doped lead-salt structured nanocrystal. 14

2.10 Band gap energy versus Mn-content for a $Pb_{1-x}Mn_xS$ alloy. 15

2.11 Dependence of the exciton recombination energy on Mn-content. . . 15

2.12 Temperature dependence of the exciton recombination energy on Mn-content. 16

2.13 Dependence of the temperature coefficient, $\alpha_{QD} = dE_{QD}/dT$, on Mn-content. 17

2.14 Optical window for biological tissues. 18

3.1 Schematic diagram of the PL mechanism in a direct band gap bulk semiconductor. 21

3.2 Schematic of experimental setup used in PL studies. 22

3.3 Schematic of experimental setup used in micro-PL studies. 23

3.4 Schematic diagram of Rayleigh and Raman Scattering. 25

3.5 Energy level splitting due to applied magnetic field and EPR absorption spectra for an unpaired electron. 27

3.6 Splitting due to applied magnetic field and EPR absorption spectra. 27

3.7 Schematic of AFM system and picture of the system used at the University of Nottingham. 30

4.1 HRTEM images of $Pb_{1-x}Mn_xS$ nanoparticles with $x = 10$ %. . . . 33

4.2 AFM images of $Pb_{1-x}Mn_xS$ nanoparticles with $x = 0$ and 10 % . . 34

4.3 EDX spectrum of $Pb_{1-x}Mn_xS$ nanoparticle with x=10 % (a) and Mn-content measured by EDX versus the nominal Mn-content (b) . 35

4.4 Normalised PL spectra of QDs with x from 0 to 18 %. 36

4.5 Dependence of the exciton recombination energy, E_{QD}, on x at $T = 295$ K 38

4.6 Mn-content as estimated from EDX and from calculated and measured values of E_{QD} 38

4.7 QD and Mn-related PL emission for $x = 7\,\%$ at $T = 295$ K 39

4.8 Temperature dependence of the PL properties for PbS nanoparticles. 40

4.9 Temperature dependence of the PL properties for $Pb_{1-x}Mn_xS$ nanoparticles with $x = 8\,\%$. 41

4.10 Temperature dependence of the FWHM for $Pb_{1-x}Mn_xS$ nanoparticles with Mn-content $x = 0$, 1.5 and 5 % 42

4.11 Temperature dependence of the PL peak position of $Pb_{1-x}Mn_xS$ nanoparticles with x up to 15 % 43

4.12 Calculated and experimental values of the temperature coefficient $\alpha_{QD} = dE_{QD}/dT$. 44

4.13 Effect of laser power on temperature dependent PL properties . . . 45

4.14 Magnetic measurements on $Pb_{1-x}Mn_xS$ nanoparticles 46

5.1 Photoinduced PL blue-shift in $Pb_{1-x}Mn_xS$ nanoparticles with $x =$ 1 %. 48

5.2 Dependence of the energy shift, ΔE_{QD}, on Mn-content after 40 min of continuous irradiation with laser light. 48

5.3 Photoinduced blue-shift of the PL peak energy in $Pb_{1-x}Mn_xS$ nanoparticles. 49

5.4 Effect of oxygen-free environment on the photoinduced PL peak energy shift. 50

5.5 Optical image and corresponding PL spectra showing damage to the nanoparticle film at high laser power densities. 51

5.6 Photoinduced PL enhancement in $Pb_{1-x}Mn_xS$ nanoparticles. . . . 53

5.7 (a) Photoinduced PL intensity enhancement in vacuum and in air and (b) partial reversibly of the PL intensity enhancement. 53

5.8 Photoinduced quenching of the Mn-related emission for doped $Pb_{1-x}Mn_xS$ nanoparticles with $x = 12$ %. 55

5.9 Graph showing the effect of laser excitation wavelength on the Mn-related PL emission. 56

5.10 Cartoon showing the photo-oxidation process in Mn-doped PbS QDs. 57

5.11 (a) Raman spectra for PbS nanoparticles over 30 min continuous illumination and (b) corresponding PL spectra. 59

5.12 Raman spectra for $Pb_{1-x}Mn_xS$ nanoparticles ($x = 3$ %) over 85 min continuous illumination (a). Corresponding PL spectra (b). Normalised Raman and PL intensity versus time, t_L, (c) 60

5.13 Raman spectra for $Pb_{1-x}Mn_xS$ ($x = 5$ %) nanoparticles over 125 min continuous illumination (a). Corresponding PL spectra (b). Normalised Raman and PL intensity versus time t_L, (c). 61

5.14 Effect of Mn-content on Raman peaks. 62

5.15 PbS LO optical phonon Raman peak versus the effective Mn-content 62

List of Tables

2.1 Comparison of the physical properties of PbS and MnS. 7

Chapter 1

Introduction

Nanostructures have attracted a great deal of attention in recent decades as materials can acquire new and interesting properties at this scale, and because these properties can change with the material's size and/or shape. This is a field of research that has relevance across many different disciplines as it lies on the boundaries of chemistry, physics, biology, biochemistry and materials science.

Research in semiconductor nanocrystals, also known as quantum dots (QDs) [1], has been expanding over the last 20 years due to rapid advancements in fabrication techniques and numerous possible applications in optoelectronic devices [2]. Properties of QDs can be manipulated by changing their size, shape and composition. One property of QDs that is of particular importance is the phenomenon of quantum confinement whereby the confinement of electrons and holes in all spatial dimensions leads to discrete quantised atomic-like energy levels [3].

There are a variety of techniques used to produce semiconductor nanocrystals [4], such as lithographic processes or self assembly. One of the most successful of these techniques is colloidal chemistry, where the QDs are synthesised chemically in solution; QDs generally comprise an inorganic core coated with a layer of organic ligand molecules. The capping provides electronic and chemical passivation of surface dangling bonds and prevents uncontrolled growth of the nanocrystals. Advances in colloidal chemistry over recent years have made possible the preparation of high quality QDs with well controlled shapes, sizes and composition.

Among several semiconductor materials lead sulphide (PbS) has attracted particular interest. Bulk PbS is a narrow gap IV-VI semiconductor with a rock salt structure and a direct band gap of 0.41 eV [5]. PbS was one of the first semiconductor materials to find wide application, where it was used as the material for point contact diodes in "crystal set" radios [6]. The relatively small electron and hole masses in PbS give a large exciton Bohr radius of $R_{ex} \sim 20\,\mathrm{nm}$ thus leading to strong exciton confinement in PbS nanocrystals. Many researches are currently focusing on PbS QDs as they are optically active in the near infrared (NIR) region leading to possible future applications including in NIR optoelectronics, solar cells, spintronics and as biological labels [7].

Intentional incorporation of impurities, or doping, has long been established as a powerful tool for controlling the properties of bulk semiconductors and has been essential in the development of semiconductor technologies. The prospect of further tailoring the electronic, optical and magnetic properties of QDs has stimulated efforts to dope semiconductor nanocrystals. Despite some difficulties, such as the self-purification of dopants to the nanocrystals' surface [8], there have been many significant advances made in this sub-field. Transition metals such as manganese (Mn) are often used as dopants as they are optically active and can also imprint semiconductor nanocrystals with magnetic properties with possible applications for spintronics [9] and as contrast agents in magnetic resonance imaging (MRI) [10].

This report will present an experimental study into how the magnetic and optical properties of colloidal PbS nanocrystals are affected by the controlled incorporation of Mn impurities. It is hoped that these nanocrystals may in the future be employed in multimodal medical imaging. Their magnetic properties make them potentiality useful as MRI contrast agents and their NIR emission (at wavelengths that are only weakly absorbed by biological tissues) make them possible candidates for fluorescent biolabels.

Chapter 2 describes the properties of the bulk materials PbS and MnS, introduces some important concepts needed for a greater understanding of some of the mechanisms observed in this work, and covers some relevant recent literature.

Chapter 3 describes the synthesis of the nanoparticles and the experimental setup and procedure used in this study. These include photoluminescence spectroscopy,

Raman spectroscopy, electron paramagnetic resonance (EPR) spectroscopy and microscopic techniques.

Chapter 4 demonstrates the effects of the Mn doping on the physical properties of PbS nanoparticles. This will include their size, shape and composition, their PL properties, temperature dependent PL properties and magnetic properties.

Chapter 5 explores some photoinduced phenomena in Mn-doped PbS nanoparticles. This will include the observation of a photoinduced blue-shift of the PL emission, enhancement of the PL intensity and the appearance of Raman lines. It will then go on to discuss some possible mechanisms that can account for these phenomena.

Chapter 6 presents a conclusion of this report and gives prospects for future investigations.

Chapter 2

Background

This chapter will give some background information on the properties of the materials used in this study. It will then introduce some important concepts such as the density of states, the exciton and quantum confinement. Understanding these concepts will be essential in gaining greater insight into the physical properties of $Pb_{1-x}Mn_xS$ nanoparticles. The chapter will then cover some literature in the subject to give an overview of the field and some recent advances.

2.1 Properties of Bulk Lead Sulphide and Manganese Sulphide

2.1.1 Bulk Lead Sulphide

Lead chalcogenides i.e. lead selenide (PbSe), lead telluride (PbTe) and lead sulphide (PbS), play a major role in infrared optoelectronics. They are characterised by narrow band gaps and large dielectric constants, and share similar band structure [11]. This report will focus on Mn-doped PbS QDs so it will be important to understand the bulk properties of PbS and manganese sulphate (MnS), which are described below.

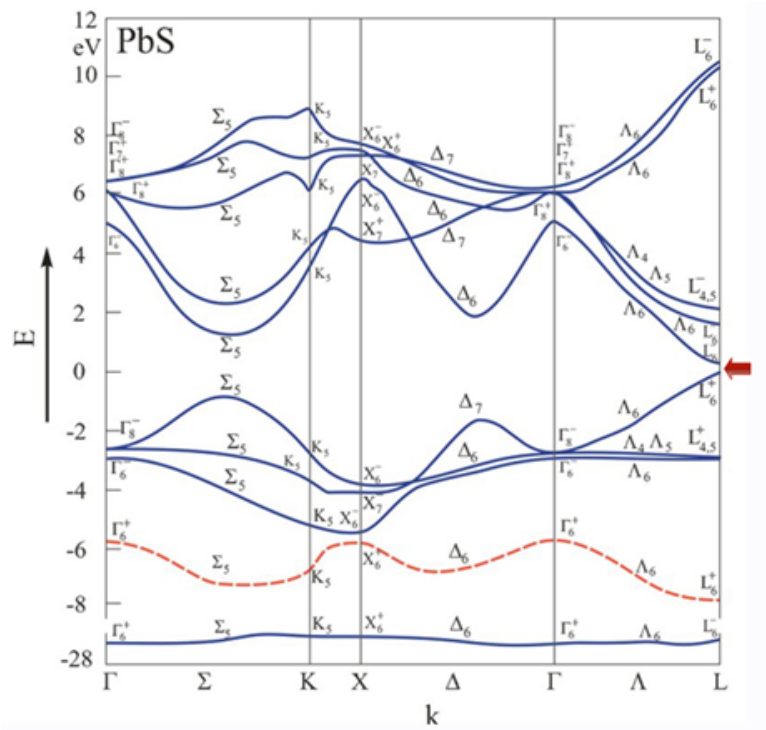

Figure 2.1: Band structure of bulk PbS reproduced from reference [12].

PbS is a IV-VI semiconductor with a direct narrow band gap of $E_g = 0.2586\,\text{eV}$ at 4 K and 0.41 eV at room temperature [12]. The conduction and valence band extrema are at the L-point of the first Brillouin zone. The band structure of PbS is shown in Figure 2.1 where the red arrow highlights the position of the conduction band and the valence band at the L-point. PbS has a rock salt or face centred cubic (fcc) lattice structure with a lattice constant of $a = 5.963\,\text{Å}$. The first Brillouin zone of such a structure is shown in Figure 2.2. It also has large dielectric constants $\varepsilon_r(0) = 169$ and $\varepsilon_r(\infty) = 17.2$ [12]. The reduction in E_g as the temperature decreases means that $dE_g/dT = +0.52$ meV/K. The positive nature of this value is interesting as it is unique to lead chalcogenides.

PbS has an exciton Bohr radius of $R_{ex} = 20\,\text{nm}$ arising from the effective electron and hole masses, which are relatively small and approximately equal: $m_e^* \approx m_h^* \approx 0.09m_0$, where m_0 is the electron mass in vacuum. This Bohr radius is large when compared to that of many other materials (e.g. CdS $\approx$ 3 nm) and leads to the strong confinement of both electrons and holes in nanocrystals where the QD radius is less than that of the Bohr radius.

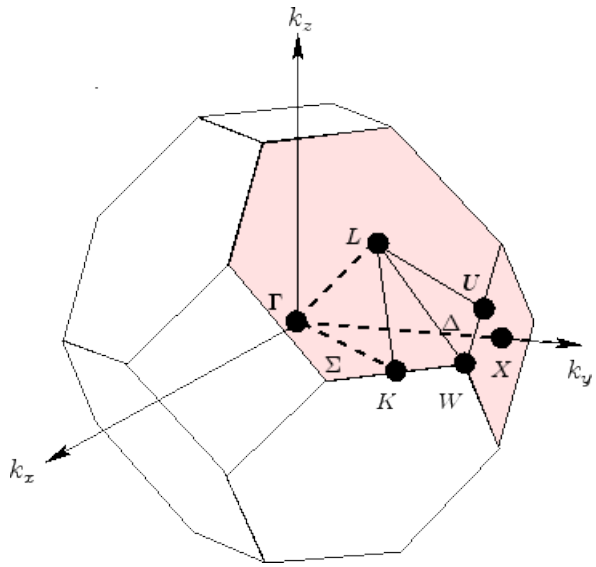

Figure 2.2: First Brillouin zone of an fcc lattice reproduced from reference [12].

Lead chalcogenides have found uses in several semiconductor devices including infrared LEDs, photovoltaics, lasers and photodetectors [11]. PbS was used in the first infrared photodetectors at the turn of the 20th century, and today the most common application for bulk PbS is still in photodetectors.

2.1.2 Manganese and Bulk Manganese Sulphide

It is important to understand manganese (Mn) atoms as these will be used to dope our PbS nanocrystals. The high levels of doping in this study also make it useful to understand the properties of bulk MnS as the alloy (PbMn)S can be formed. This is because Mn has a strong preference for occupying the Pb-site in the crystal lattice [13].

Mn is a transition metal with the atomic number 25, with electron configuration [Ar] $4s^2$, $3d^5$. It can exhibit a number of oxidation states +2, +3, +4, +6, and +7. Mn has five unpaired electrons in the d-shell, making it an excellent candidate as a dopant as its magnetic properties can be incorporated into PbS.

MnS is a magnetic, direct ultra wide gap semiconductor with a band gap of $E_g = 3.2\,\mathrm{eV}$ and a temperature coefficient $dE_g/dT = -2\,\mathrm{meV/K}$ [14]. Table 2.1 shows

a comparison of some of the important properties of bulk MnS and PbS. PbS and MnS have a similar rock-salt crystal structure and lattice constant, however their band gap energies and the coefficient dE_g/dT are drastically different. Unlike PbS, bulk MnS is not a commonly used material in semiconductor technologies due to its wide band gap, and its growth being a much more difficult process [15].

	PbS	**MnS**
$\boldsymbol{a}$	5.9 Å	5.2 Å
$\boldsymbol{E_g}$ **(at 300 K)**	0.41 eV	3.2 eV
$\boldsymbol{dE_g/dT}$	0.52 meV/K	−2 meV/K

Table 2.1: Values of lattice constant (a), band gap energy (E_g) and dE_g/dT in PbS [12] and MnS [14].

2.2 Quantum Confinement

Here we must first cover some core concepts, which will in turn enable us to gain an understanding of how quantum confinement effects the properties of quantum dots. Two concepts that must be introduced are that of the density of states (DOS) and the exciton.

First we will introduce the concept of the DOS. The DOS of a system describes the number of electronic states that are available to be occupied per interval of energy [16]. It can be shown that for a 3D system with volume L^3 and parabolic energy dispersion that the DOS per unit volume is given by:

$$D(E) = \frac{m_e^* \sqrt{2m_e^* E}}{\pi^2 \hbar^3}, \tag{2.1}$$

where m_e^* is the effective electron mass, E is the energy and $\hbar$ is the reduced Planck constant. Here the DOS is proportional to $E^{1/2}$ and the electron can occupy a continuum of energy levels as shown in Figure 2.3.

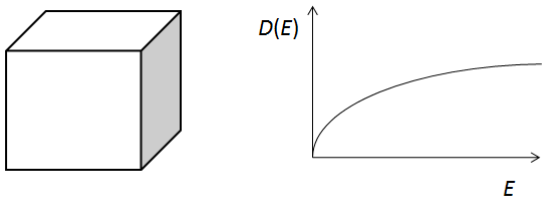

Figure 2.3: DOS for a 3D system.

For a 2D system where the electron is confined in one spatial direction and allowed to move freely in the other two directions, the DOS can be shown to be:

$$D(E) = \frac{m_e^*}{\pi\hbar^2}. \tag{2.2}$$

In this case the DOS is independent of E, which leads to a constant density of states. For a quasi 2D system (i.e a quantum well) the electron is free to move in xy and quantised in z. This produces a series of 2D energy subbands, and a step-like dependence of the DOS. Equal height staircases correspond to different subbands, as seen in Figure 2.4.

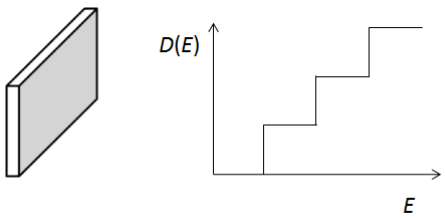

Figure 2.4: DOS for a quantum well.

For a 1D system where the electron is confined in two spatial directions the DOS is given by:

$$D(E) = \frac{1}{\pi\hbar}\sqrt{\frac{2m_e^*}{E}}. \tag{2.3}$$

In this case the DOS is proportional to $E^{-1/2}$ and resembles a spike. For a quasi 1D system (i.e a quantum wire) subbands similar to those described in the 2D system occur and this leads to a series of spikes as shown in Figure 2.5.

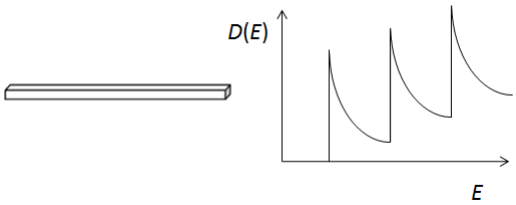

Figure 2.5: DOS for a quantum wire.

For a 0D system (i.e. quantum dot) the electron motion is quantised in all three spatial directions as seen in Figure 2.6. All the states exist only at discrete energies and can be represented by delta functions.

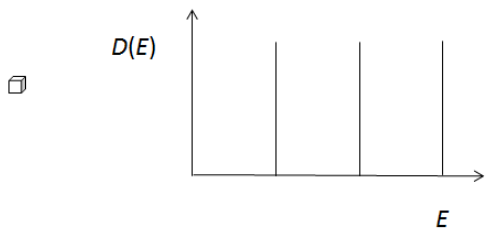

Figure 2.6: DOS for a quantum dot.

Another important concept in semiconductor physics is the exciton. In semiconductors the exciton is a bound electron-hole pair that is created by the absorption of a photon. The newly formed electron-hole pair or exciton is bound together by the Coulomb interaction. Due to this attraction the energy required for the exciton to be created is slightly lower than the band gap of the semiconductor (see Figure 2.7). After some time the electron and hole will recombine, the exciton will vanish and a photon will be emitted from the material. A convenient analogy that can help to understand this concept is that of the well understood hydrogen atom, the difference being the mass of the positive charge carriers in each case (the effective mass of the hole is much less than that of the proton). Another difference is that due to the smaller masses and the screening of the Coulomb force by the

many electrons in the system the exciton binding energy is much smaller than the binding energy in the hydrogen atom [16].

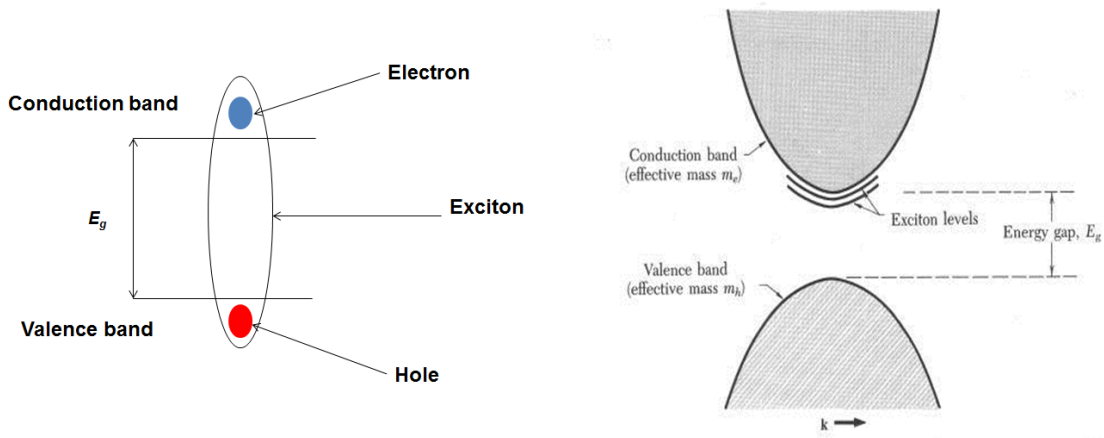

Figure 2.7: Schematic diagram of the exciton (left) and exciton energy levels (right) reproduced from Ref. [16].

The exciton can be treated in two different cases depending on the properties of the material in which the exciton exists. For materials with a small dielectric constant, the Coulomb interaction between the electron-hole pair is strong and thus the exciton is tightly bound and the radius small, and comparable to the lattice constant. These are known as Frenkel excitons [16]. In the case where the dielectric constant is large (i.e. semiconductors) the Coulomb interaction is reduced, the electron-hole pair is less tightly bound, the binding energy reduced and the radius is larger than in the previous case. These are known as Wannier-Mott excitons [16]. For a 3D system the exciton binding energy is given by

$$E_{ex} = \frac{\mu e^4}{8\varepsilon_r^2 \varepsilon^2 h}, \tag{2.4}$$

and the exciton Bohr radius is given by

$$R_{ex} = \frac{\hbar^2 \varepsilon_r}{\mu e^2}, \tag{2.5}$$

where $\mu^{-1} = m_e^{*-1} + m_h^{*-1}$ is the reduced mass of the electron and hole pair. The binding energy is much greater when confinement effects are present.

The concepts of the DOS and the exciton covered in the previous few paragraphs will now enable us to gain a greater understanding of how quantum confinement effects QDs.

Quantum confinement causes a change in the properties, both optical and electronic, of a material when that material is of sufficiently small size. Confinement effects occur when electrons and holes are squeezed into a dimension that approaches the exciton Bohr radius [17]. As the size of the nanostructure decreases, the confinement effects become stronger and the band gap of the semiconductor increases (blue-shifts). The first experimental evidence of the quantum confinement effects in clusters came from crystalline CuCl grown in silicate glasses in 1982 [18]. Quantum confinement is a direct consequence of quantum mechanics and cannot be explained classically.

There are a number of models that attempt to describe how confinement affects QD energy levels as their size changes [19, 20, 21]. This study uses a simple spherical model, that builds on the previous model proposed by Brus in 1986 [21] by taking into account the hyperbolicity of the conduction and valence bands in PbS [5]. This model describes the ground exciton energy as:

$$E_{QD} = \sqrt{E_g^2 + \frac{2\hbar E_g \pi^2}{m^* R^2}}, \tag{2.6}$$

where m^* is the average of the electron and hole effective masses, and R is the QD radius.

PbS has large Bohr radius of $R_{ex} = 20\,\text{nm}$, which means that strong confinement effects are much more easily achieved than in other materials. Figure 2.8 shows the calculated value of E_{QD} versus R at $T = 300$ K according to equation 2.6 with energy $E_g = 0.41$ eV and $m^* = 0.09 m_e$. It can be seen that a strong confinement effect occurs for $R < 10$ nm.

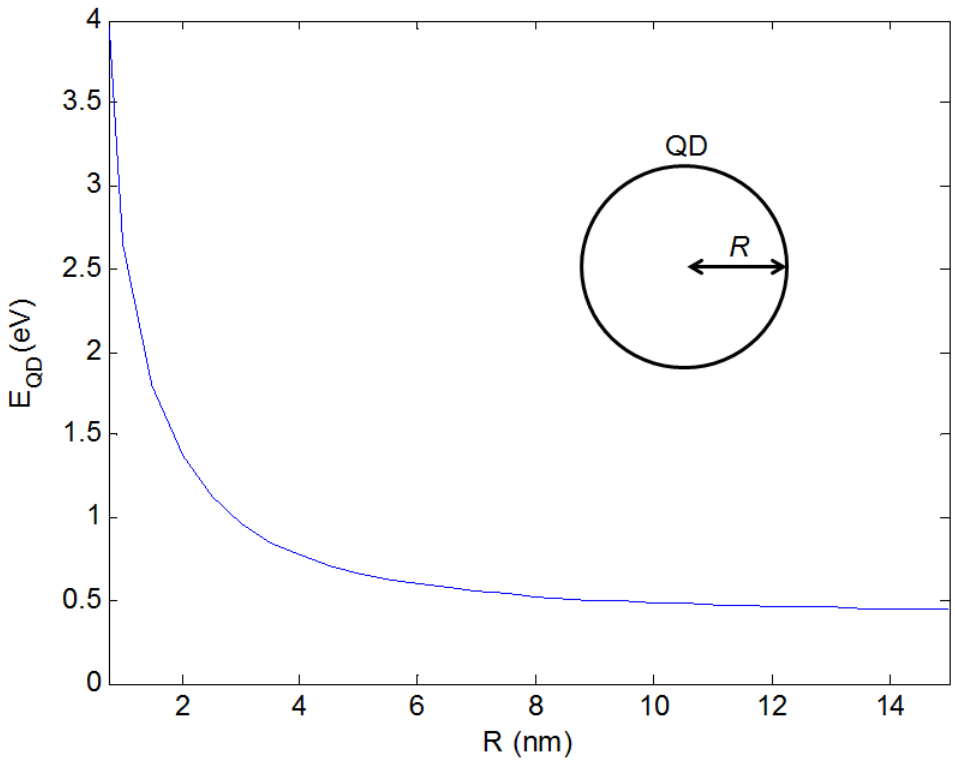

Figure 2.8: Graph showing the dependence of E_{QD} on the PbS nanocrystal radius R modelled using a simple spherical model where $E_g = 0.41\,\text{eV}$, $T = 300$ K and $m^* = 0.09m_e$ is the average effective mass.

2.3 Mn-doped PbS Colloidal Quantum Dots

There are three major methods of producing quantum dots: by advanced lithographic techniques, by epitaxial techniques or by colloidal chemistry [17]. Advanced lithographic processes are used to fabricate a 2D structure that can then be etched down to create a QD, however these QDs are limited by the spatial resolution of the lithography [22]. Epitaxial techniques such as molecular beam epitaxy (MBE) can be used to produced so called 'self-assembled' QDs whereby two semiconductors with different lattice spacing are grown on top of each other. The strain caused by this lattice mismatch produces 'islands' of quantum dots on top of a 2D wetting layer. This method is limited by the randomness of the positions of individual QDs on the substrate [23].

The QDs studied in this report are produced by colloidal chemistry. In this method the inorganic semiconductor nanocrystals are grown in solution and then capped by a layer of organic ligand molecules which prevents uncontrolled growth and stabilises their shape and composition [24, 1] by electronic and chemical passivation of surface dangling bonds. This organic capping layer assists with solubility and makes QDs fabricated by colloidal chemistry ideal for medical applications [25]. There are several other advantages of colloidal chemistry including the fact that production is relatively cheap when compared to the other methods that require more advanced technologies. Over recent years greater and greater control over the composition, size, shape, structure and surface properties have been achieved during synthesis. High quality colloidal QDs can be routinely produced by many research groups and commercial companies around the world.

Lead chalcogenides PbX are attracting attention as strong confinement can be achieved relatively easily due to their large exciton Bohr radius and also due to their narrow band gaps which make them optically active in the infrared (IR) and NIR regions making them possible candidates for numerous applications [26, 27, 28, 29]. These applications include optoelectronics [26], solar cells [27], materials in field effect transistors [28] and as fluorescent biolabels [29]. Colloidal PbS QDs have been produced in a variety of different ways with an assortment of different capping agents used to stabilise the properties and assist with the functionalisation of the dots [24].

Recent studies on PbS QDs show excellent control of the size and shape of the nanoparticles and thus control of their optical properties, with their emission tunable in the range $800 - 1800\,\mathrm{nm}$ [7]. Optical properties of both colloidal and self assembled PbS QDs have now been well studied under various conditions with the effects of temperature dependence [30, 31], magnetic field dependence [32, 33] and excitation power dependence [34] on their PL being investigated. A number of different capping layers and their effects on the properties of PbS have also been widely studied . Despite various research groups studying these nanocrystals there are still many challenges remaining in understanding the physical mechanisms within such complex systems.

An active area of research within this field is the modification of the QD properties by the controlled incorporation of dopants [35]. There are two major categories of dopants for semiconductor nanoparticles: that of luminescence activators and

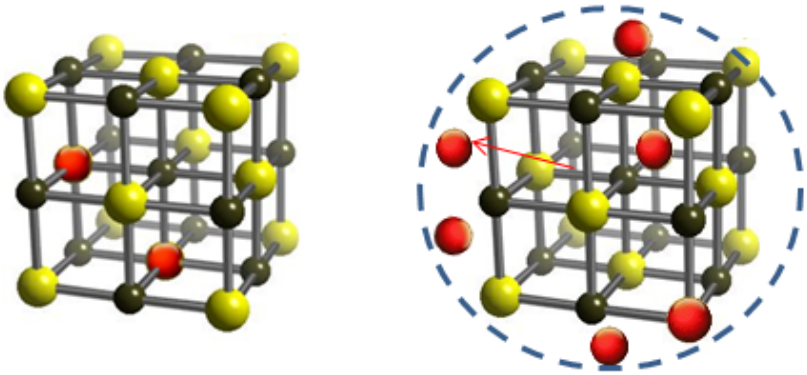

Figure 2.9: Cartoon showing self-purification process for a doped lead-salt structured nanocrystal.

magnetic ions used to imprint the nanocrystal with magnetic properties [36]; these two functions can often be achieved with the same dopant material. There are many obstacles to overcome when attempting to prepare doped QDs. One major issue is that the host materials have a huge surface/volume ratio. Because of this nanocrystals have a tendency to 'self-purify' whereby dopants diffuse out of the nanocrystal core towards the surface [8], see Figure 2.9. Alongside this process another problem is that an ensemble of nanocrystals will possess a wide range of dopant ion populations creating inhomogeneity within the ensemble [37].

To date there are various reports of Mn-doped PbS QDs supported in a glass matrix [38, 39], however there are very few examples of these nanocrystals produced by colloidal chemistry [40].

Previous theoretical reports suggest that the Mn ions have a strong preference for occupying the Pb lattice sites in the rock salt crystal structure [41]. This and the relatively high levels of Mn used in doping can lead to the formation of alloyed $Pb_{1-x}Mn_xS$. Vegard's law is an empirical rule proposed by Vegard in 1921 [41] which holds that at a constant temperature there is a linear relation between the crystal lattice parameter and alloy composition. In semiconductors this relation can be extended to determine semiconductor band gap energies. If we consider the example of bulk $Pb_{1-x}Mn_xS$, then Vegard's law states:

$$E_g^{Pb_{1-x}Mnx} = (1-x)E_g^{PbS} + xE_g^{MnS}. \tag{2.7}$$

This law can be use to calculate the exciton recombination energy, E_{QD}, for QDs if the simple spherical model described by equation 2.6 in the previous section is used to account for the confinement effects. Figure 2.10 shows the band gap energy versus x for a $Pb_{1-x}Mn_xS$ alloy with x up to 20 %, where we have assumed $E_g^{PbS} = 0.41\,\text{eV}$ and $E_g^{MnS} = 3.2\,\text{eV}$ at $T = 300$ K. Figure 2.11 shows the value of E_{QD} versus x for $Pb_{1-x}Mn_xS$ nanoparticles, calculated with the model described in the previous section with $m^* = 0.09m_e$, $R = 2.5\,\text{nm}$ and $T = 300$ K.

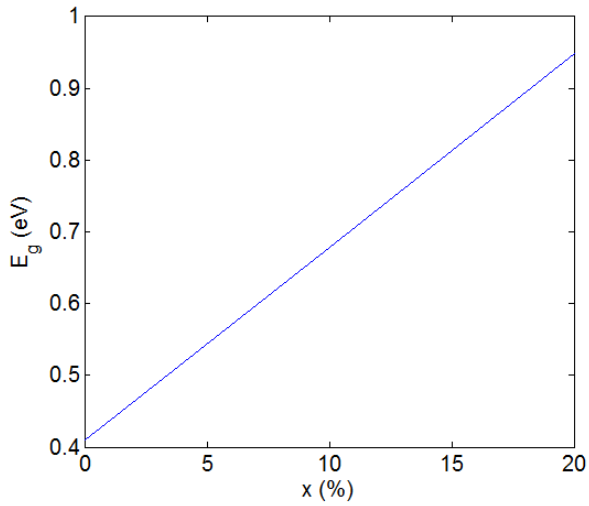

Figure 2.10: Band gap energy, E_g, versus Mn-content, x, for a bulk $Pb_{1-x}Mn_xS$ alloy at $T = 300$ K.

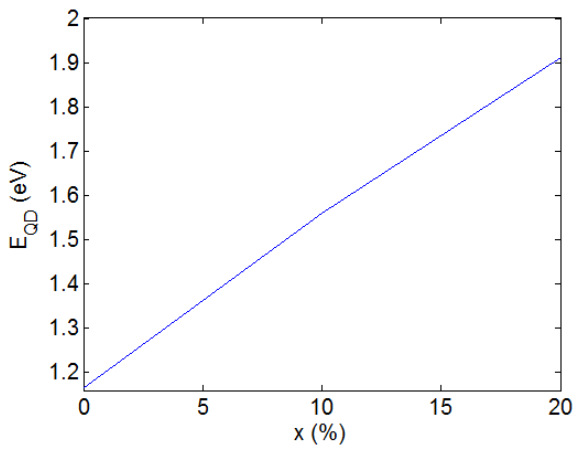

Figure 2.11: Dependence of the exciton recombination energy, E_{QD}, on Mn-content, x, for $Pb_{1-x}Mn_xS$ nanoparticles, with radius $R = 2.5$ nm at $T = 300$ K.

Vegard's law can also be used to model the thermal dependence of the QD recombination energy, i.e $\alpha_{QD} = dE_{QD}/dT$. Using the model described in the previous section [5] it can be shown that:

$$\frac{dE_{QD}}{dT} = \alpha_{QD} = [\alpha_{PbS}(1-x) + x\alpha_{MnS}] \left\{ \frac{2E_g(x) + \hbar^2 R^{-2} m^{*-1}}{2E_{QD}} \right\} \tag{2.8}$$

where $E_g(x) = E_{PbS}(1-x) + xE_{MnS}$. This equation can now be used to model the temperature dependence of E_{QD} and the dependence α_{QD} on the Mn-content, as shown in Figure 2.12 and 2.13. Here we have assumed $\alpha_{PbS} = +0.52$ meV/K [12] and $\alpha_{MnS} = -2$ meV/K [14] for $T > 100$ K. Interestingly, this model predicts that for $x \sim 20$ %, $\alpha_{QD} = 0$ thus indicating that the exciton recombination energy should be independent of the temperature.

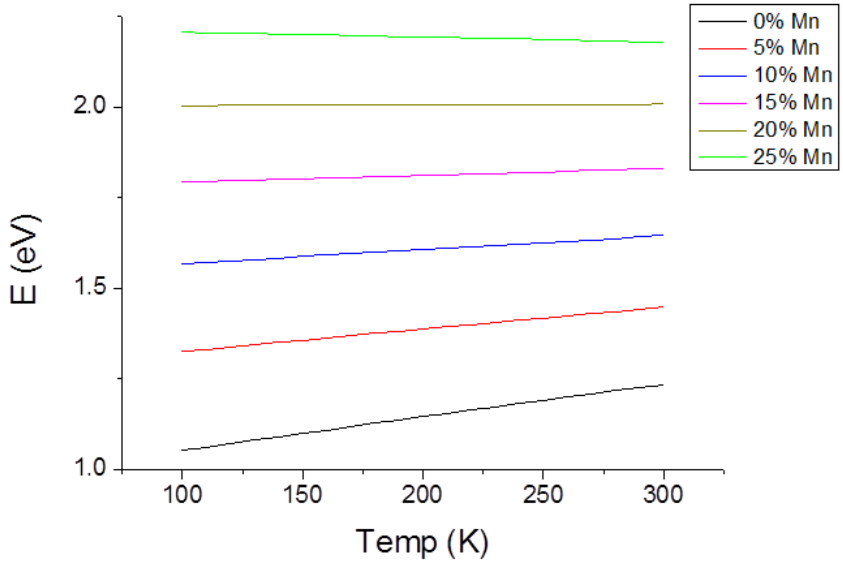

Figure 2.12: Temperature dependence of E_{QD} using Vegard's law and a simple spherical model for $Pb_{1-x}Mn_xS$ nanoparticles with radius $R = 2.5$ nm for Mn-content up to 25 %.

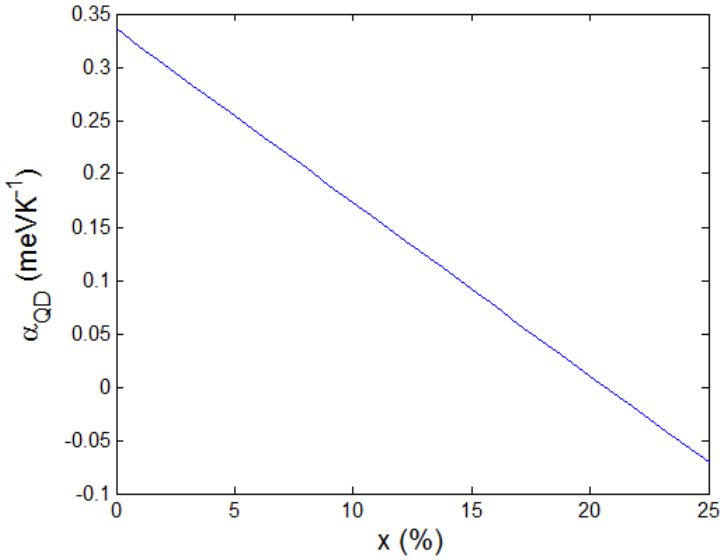

Figure 2.13: Dependence of $\alpha_{QD} = dE_{QD}/dT$ on the Mn-content using Vegard's law and the simple spherical model for $Pb_{1-x}Mn_xS$ nanoparticles with radius $R = 2.5$ nm for Mn-content up to 25 %.

2.4 QDs as fluorescent biolabels and MRI contrast agents

Optical imaging has become an important tool in biological and biomedical research. Traditionally imaging relies on single-photon emitting organic dyes, which are widely used for the imaging of biological samples [42]. One of the major problems associated with optical imaging is that biological tissues strongly absorb light in the visible region. This makes it necessary for labels to emit light in the NIR region dubbed the 'optical window' or 'therapeutic window' [43] where light of these wavelengths are only weakly absorbed by biological tissues, see Figure 2.14.

Colloidal QDs have many advantages over dyes for medical optical imaging: they absorb light over a wide range of wavelengths unlike standard chemical fluorophores [25]; they have photostability which is several orders of magnitude greater than that of conventional dyes [43]; also their emission is tunable and can be carefully controlled as previously mentioned.

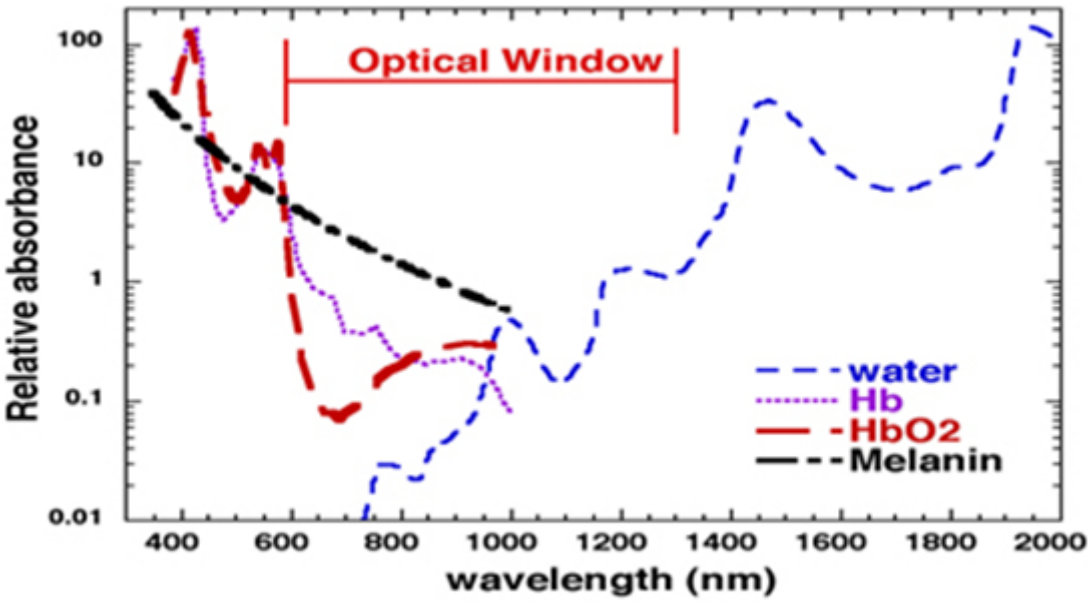

Figure 2.14: Optical window for biological tissues. Hb: Haemoglobin. HbO_2 Oxygenated haemoglobin. Reproduced from reference [44].

MRI has become an essential tool in medical research and diagnostics since the first scanners became available to the medical profession in the 1980s [45]. To increase the sensitivity of detection in MRI contrast agents must be used. Great efforts are being made to improve classical contrast agents, such as paramagnetic ion complexes and superparamagnetic iron oxide particles [46]. However, nanoscale magnetic materials are now also attracting a great deal of attention as their size and shape can be manipulated to a great degree of accuracy and they have the possibility of becoming multifunctional as optical imaging agents and/or as drug delivery systems [47, 48].

The ultimate goal would be to utilise QDs in a clinical setting, but many concerns have been raised about their toxicity due to their heavy metal content [49]. Because of this, efforts are being made to enhance their biocompatibility. There have been various recent studies that suggest that if QDs are coated properly with the right organic ligands, they can be made non toxic or their toxicity can be greatly reduced [50, 51]. As there are many types of QDs, each with a different chemical make-up, they will need to be characterised individually to asses their potential toxicity. There will, of course, need to be many more systematic studies and trials completed before QDs find a routine role in clinical medicine.

Chapter 3

Synthesis and Experimental Techniques

In this chapter the synthesis of the nanoparticles and the experimental techniques used to study them are described. Measurements were performed at The University of Nottingham and the National EPR Research Facility and Service at the University of Manchester.

3.1 Synthesis

Colloidal Mn-doped PbS nanoparticles were synthesised using a similar method to the one proposed by Levina *et al* [52] where thioglycerol (TGL) and dithioglycerol (DTG) are used as capping agents. These are organic compounds that have a functional group of sulphur and hydrogen atoms, and bind to the nanoparticle surface with a hydrogen bond. Synthesis of the samples discussed in this report was performed at the University of Nottingham by Dr. L. Turyanska.

To synthesise the nanoparticles, a Pb^{2+} precursor solution was prepared containing 2.4×10^{-4}mol of lead acetate $Pb(CH_3COO)_2$, 1.5×10^{-3}mol of TGL and 5×10^{-4}mol of DTG in 15 mL of deionized water. The pH of the solution was adjusted to a value of 11.0 by addition of triethylamine. While maintaining the pH

of the solution, manganese acetate $Mn(CH_3COO)_2$ salt was added with nominal Mn-concentration, x, up to 18%. To facilitate the incorporation of the Mn-atoms during the nucleation stage of the nanocrystal growth, a 0.1 mol solution of sodium sulphide Na_2S was added slowly to the reaction mixture at a molar ratio MR = 1:0.3 of Pb(Mn) to S. The outcome is a brown colloidal solution of thiol-capped PbS QDs [53]. The synthesis was performed under N_2 flux and the final solutions stored in a fridge at $T = 4\,°C$ under N_2 atmosphere. This oxygen-free environment prevents the oxidation of the samples and sedimentation phenomena. Fresh solutions were prepared regularly to maintain the availability of good solutions. After the synthesis, the solutions were left to rest for ∼7 days to stabilise the formation of the nanocrystals.

3.2 Photoluminescence

In semiconductors luminescence is a radiative recombination process involving electrons and holes [54, 55]. An electron-hole pair or exciton are created due to an excitation, the carriers then recombine and a photon is emitted from the system. This excitation can be thermal, electrical or optical. If the excitation is thermal, the process is known as thermoluminescence, if it is electrical then the process is known as electroluminescence, and if it is optical then the process is known as photoluminescence (PL) [54]. This section will describe the mechanism for photoluminescence and the experimental setup used to measure photoluminescence at the University of Nottingham.

In semiconductors when an electron in the valence band is excited by a photon of energy greater than the band gap, the electron moves higher into the conduction band. The carrier then relaxes to the conduction band minimum rapidly losing energy via phonons (quantised lattice vibrations). There is a similar mechanism for holes whereby they relax to the valence band maximum, these processes are known together as carrier relaxation [55, 54]. Carrier relaxation is much faster than the recombination of electrons and holes [55] therefore the charge carriers will relax to the bottom or top of the conduction or valence bands before recombination. When the carriers recombine a photon will be emitted with energy equal to that of the band gap. Figure 3.1 shows a schematic diagram of the PL process in a bulk direct band gap semiconductor. Similarly, in QDs carriers relax to the lowest discrete

energy level and will emit a photon of energy E_{QD}. Carrier relaxation among the discrete states of the QDs may involve Auger processes thus preventing the so called 'phonon bottleneck' [56]. The inhomogeneity in real systems due to structural defects in the lattice and impurities in the composition of the material can significantly affect the material's PL properties, i.e the PL peak energy, optical linewidth and intensity [57].

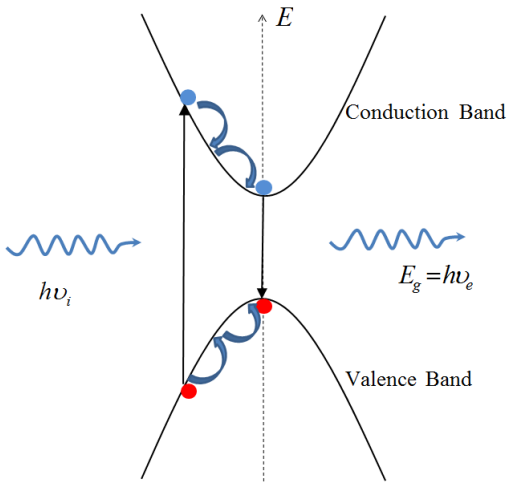

Figure 3.1: Schematic diagram of the PL mechanism in a direct band gap bulk semiconductor.

PL is a useful tool as it provides a contactless, non-destructive method to probe the optical and electronic properties of semiconductor materials. PL spectroscopy has a simple experimental setup, which can be used to estimate the band gap energy, defect/impurity detection and to look at recombination mechanisms. In QDs these experiments can also give us important information about how quantum confinement affects optical and electronic properties. The relative simplicity of the experimental setup means that the experiment can also be performed at low temperatures. This allows for in depth studies of the temperature dependence of the PL properties to be made.

The most common source for excitation in PL experiments are lasers. Lasers produce intense, monochromatic light making them an excellent excitation source. The power of the laser beam can also be adjusted using optical density filters therefore the power dependence of a materials PL properties can easily be measured.

3.2.1 PL Experimental Setup

PL measurements at the University of Nottingham were made on two systems. In the first system the excitation is provided by either a He-Ne laser ($\lambda = 633\,\text{nm}$) with power up to 5 mW or with an Argon laser ($\lambda = 514\,\text{nm}$) with power up 2 2 mW. The laser spot is focused down to 0.1 mm using conventional glass lenses. In the experiments on this system the laser power densities were varied over the range $0.01 - 10\,\text{W/cm}^2$.

For photon detection in the range $400 - 1100\,\text{nm}$, a 0.5 monochromator and liquid nitrogen cooled charge coupled device (CCD) detector is used; for wavelengths in the range $800 - 1500\,\text{nm}$, a liquid nitrogen cooled InGaAs detector is used. The detectors used here produce background signal and noise, which are reduced by the nitrogen cooling. To further assist with noise reduction, the computer software is used to controlled the detection system can subtract the background noise.

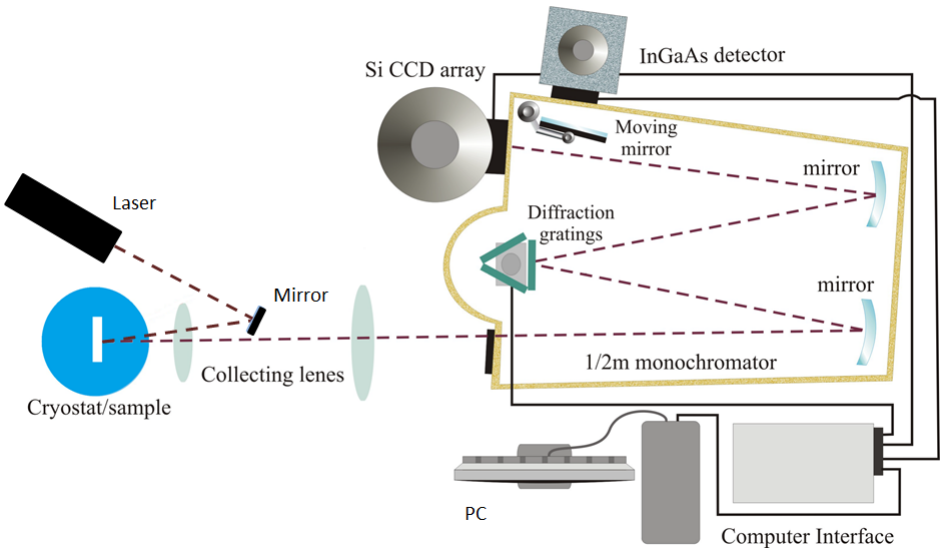

Figure 3.2: Schematic of experimental setup used in PL studies.

For low temperature and temperature dependence studies the samples are placed in an Oxford Instrument continuous gas-flow cryostat. Cooling is provided by helium gas pumped from a liquid helium Dewar, which is connected via a transfer line, the pump being used to control the flux of helium into the cryostat. Temperature within the cryostat can be controlled with an Oxford Instrument temperature controller connected to a rhodium iron thermometer and heater. Temperatures

can be controlled in the range $3.5 - 300\,\mathrm{K}$ to within $< 1\,\mathrm{K}$. The samples are excited within the cryostat through a vacuum sealed optical window on the front of the cryostat. The window comprises of two quartz layers one on the outside of the vacuum space and one on the inside connected the sample cavity. Figure 3.1 shows a schematic diagram of the PL system.

The second system is a Horiba Jobin Yuon Ltd.(HR800) Lab. Ram. This is an integrated system designed for Raman spectroscopy and micro-PL studies. The system comes equipped with a He-Ne laser ($\lambda = 633\,\mathrm{nm}$) with a power at the source of up to $14\,\mathrm{mW}$. In addition, the system has been modified to include a solid state laser ($\lambda = 532\,\mathrm{nm}$) with power at the source of up to $300\,\mathrm{mW}$. Both can be used for excitation in PL studies. Both laser beams reach the sample through a microscope fitted with 3 objectives, $10\times$, $50\times$ and $100\times$, corresponding to a spot diameter ranging from $\sim 3 - 1\,\mu\mathrm{m}$. The $50\times$ objective is corrected in the NIR region making it ideal for the PL studies in this report.

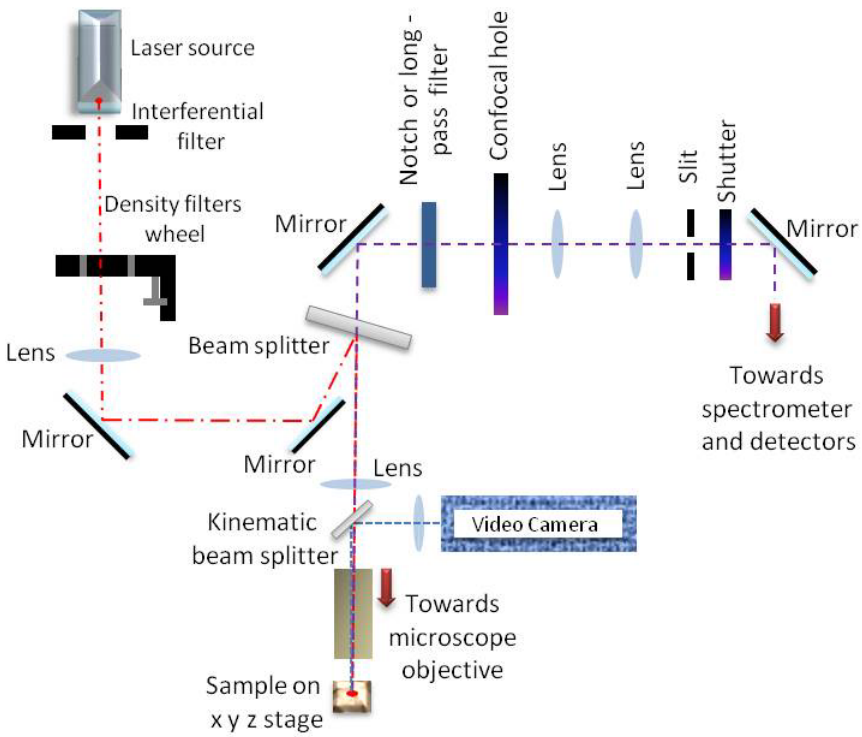

Figure 3.3: Schematic of experimental setup used in micro-PL studies.

For light dispersion, a 0.8 m spectrometer and a 1200 g/mm or 150 g/mm diffraction gratings were used. For detection in the range $200 - 1100$ nm, a Peltier cooled CCD detector was used, for wavelengths in the range $800 - 1500$ nm, a liquid nitrogen cooled InGaAs array detector was used. The PL signal is collected by the microscope objectives, then reaches a confocal hole and then on to the spectrometer and detectors. The hole can be changed between 0 and 1000 µm; reducing the hole size enhances spatial resolution but also reduces the amount of light collected. The system also comes equipped with a motorised stage which can be used for PL-mapping, and camera that can be used to obtain optical images of the sample. Low temperature experiments can also be performed in this setup. In this case the stage can be replaced with a cold-finger cryostat. Figure 3.3 shows a schematic of the micro-PL experimental setup.

3.3 Raman Spectroscopy

Raman scattering is the inelastic scattering of photons due to an excitation, it was discovered by C. V. Raman in 1928 [58]. For example in a crystal most incident photons are scattered elastically (i.e with the same energy), this is known as Rayleigh scattering. However a small proportion ($\sim 0.001\%$) are scattered inelastically as they loose or gain energy due to lattice vibrations.

In solids there are two type of Raman scattering: Stokes scattering whereby the incident photons are red-shifted as some energy is transferred to the crystal lattice via phonons, and anti-Stokes whereby incident light is blue-shifted as lattice vibrations give energy to the incident photons as shown in Figure 3.4. Anti-Stokes shift is much more unlikely than the Stokes shift therefore a much weaker signal is observed in Raman spectroscopy. The amount of scattering is determined by the vibrational modes of the bonds in a material, therefore materials have a unique Raman 'fingerprint'. This characteristic 'fingerprint' provides positive identification of unknown materials to a much greater degree than many other techniques.

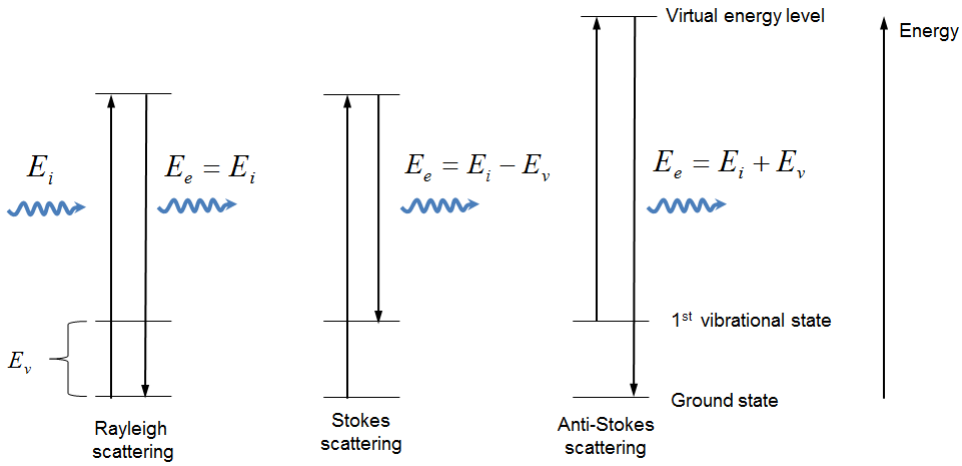

Figure 3.4: Schematic diagram of Rayleigh and Raman Scattering.

To obtain a Raman spectrum, the sample is illuminated by laser light. Since the Raman shift is independent of the excitation wavelength various different lasers can be used. As the intensity of light scattered elastically will greatly exceed the Raman scattered light it is necessary to suppress the laser light with a filter. The Raman scattered light is now collected with a lens and sent to a spectrometer to obtain a Raman spectrum.

The position of the Raman mode is conventionally measured in cm^{-1}. The laser line is taken to be the zero point and the Raman scattered light is shown as a shift from this zero point. Generally, commercial filters cut-out the spectral range of $\pm 80 - 100\,\mathrm{cm}^{-1}$, therefore not all the vibrational modes can be measured when using these filters.

For Raman spectroscopy at the University of Nottingham the Horiba Jobin Yuon Ltd.(HR800) Lab. Ram system described in the previous section was used. The excitation source used was the He-Ne laser ($\lambda = 633\,\mathrm{nm}$) and an edge filter was used to suppress the laser light. This type of filter blocks all light of wavelengths below the laser line therefore anti-Stokes shift cannot be measured in this system. For detection, the Peltier cooled CCD detector is used.

3.4 Magnetic Measurements

3.4.1 Electron Paramagnetic Resonance Spectroscopy

Electron paramagnetic resonance spectroscopy (EPR) is a versatile, non-destructive technique that can be used to study paramagnetic materials. Paramagnetic properties are due to the presence of unpaired electrons.

When an electron is placed within a magnetic field, the spin can align in two different ways: in the direction of the applied magnetic field, or opposite to the direction of the applied magnetic field. These two possible alignments have different energies, which leads to a splitting of energy levels [59] shown in Figure 3.5a. The splitting of energy levels due to an applied magnetic field is known as Zeeman splitting. For a molecule with one unpaired electron in a magnetic field the difference in energy between the two spin states, $m_s = \pm 1/2$ is:

$$\Delta E = -\frac{1}{2} g \mu_B B, \tag{3.1}$$

where g is the g-factor, μ_B is the Bohr magneton, and B is the applied magnetic field.

In an EPR experiment, a sample is exposed to gigahertz radiation, then the magnetic field is swept and absorption occurs when the magnetic field splits the energy between the two spin states to an energy that equals that of the incident radiation [59]. This is known as resonance and is how a spectrum is obtained in a EPR experiment. Unlike other spectrometers, EPR spectrometers use a phase-sensitive detector. This results in the absorption signal being represented as the first derivative, as shown in Figure 3.5b.

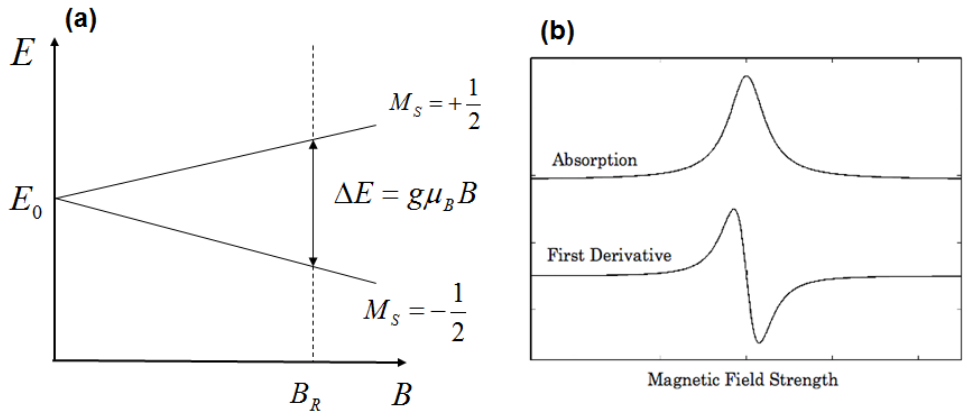

Figure 3.5: Energy level splitting due to applied magnetic field (a) and EPR absorption spectra for an unpaired electron (b).

Unpaired electrons are also sensitive to the local environment. The nuclei of the atoms in a sample have a magnetic moment, which produces a magnetic field. This additional interaction between the electrons and the nucleus is known as the hyperfine interaction. This hyperfine coupling leads to further splitting of energy levels and thus splitting of spectral lines in an EPR spectrum. The specific number, separation and relative intensities of these lines give information on the number of magnetic nuclei, their spin, I, and the strength of the hyperfine interactions.

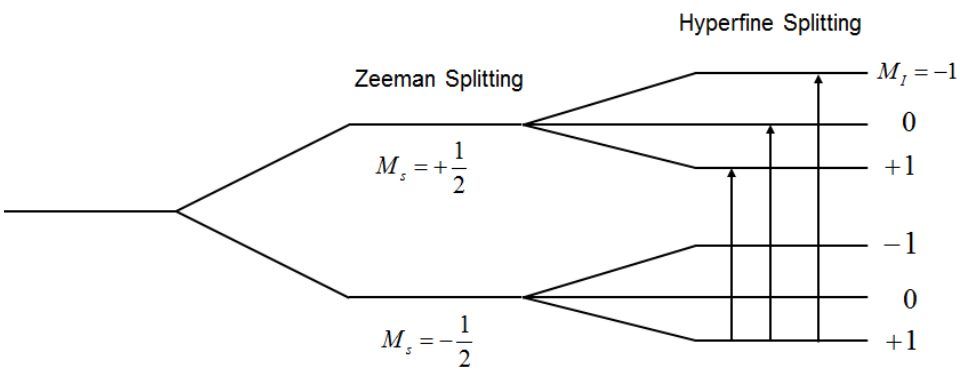

Figure 3.6: Schematic of energy levels and allowed transitions for $S = 1/2$ and $I = 1$.

EPR has been a valuable technique for determining whether or not paramagnetic dopants are incorporated into nanoparticles during the doping procedure [60, 61].

EPR measurements in this report were performed at the National EPR Research Facility and Service at the University of Manchester by Dr. Fabrizio Moro. Measurements were recorded on a commercial Bruker E580 spectrometer. Measurements were carried out at K-band (23.9 GHz), with the microwave field B_1 perpendicular to the external magnetic field B, modulation amplitude of 0.5 mT and a modulation frequency of 50 KHz.

3.4.2 SQUID Measurements

A superconducting quantum interference device or SQUID is a very sensitive device used for measuring extremely small magnetic fields the first device being made in 1964 [62] following the postulation of the Josephson effect in 1962 [63]. The SQUID consists of two superconductors separated by thin insulating layers to form two parallel Josephson junctions.

Since the magnetic moment induced in paramagnetic materials by an applied magnetic field is generality weak, sensitive devices are needed. Therefore SQUID magnetometers are often used to conduct measurements on paramagnetic materials. Their sensitivity also makes them ideal for studying the small magnetic fields produced by biological organisms.

3.5 Energy-Dispersive X-ray Spectroscopy

Energy-dispersive X-ray spectroscopy (EDX) is a powerful non-destructive technique used to identify the elemental composition of a material. The technique makes use of the X-ray spectrum that is emitted by a solid sample, which is being bombarded by a electron beam [64].

EDX uses an electron beam to stimulate emission of characteristic X-rays from a sample. The incident beam may excite an electron from an inner shell to a outer shell creating a hole in the process. Now an electron from the outer shell fills this hole and an X-ray is emitted from the material with energy equal to that of the transition between the two shells [64]. Each element has a unique atomic

structure leading to a characteristic X-ray spectrum. Thereby detailed analysis of the elemental composition of a solid material is made possible by this technique.

In this study EDX measurements were recorded with an Oxford Instrument ultrathin-window EDX detector.

3.6 Atomic Force Microscopy

Atomic force microscopy (AFM) is a scanning probe microscopy technique. The atomic force microscope was first invented by Binning in 1986 [65] and was developed to overcome some of the limitations of the scanning tunnelling microscope (STM), which was invented 5 years before [66]. It is a very powerful technique due to the very high spatial resolution (< 1 nm). Also it can, in principle, be used to probe any surface. Unlike an STM, the sample does not require any complex preparation for the technique to be performed.

The atomic force microscope consists of a cantilever with a sharp tip at its end, which is used to probe the sample. The tip is generally in the order of a few nanometres. A piezoelectric transducer is used to control the cantilever movements with high precision. The technique utilises the force between the tip (typically consisting of silicon or silicon nitrate) and the sample. When the tip is brought close to the sample's, surface the force between the tip and the sample causes the cantilever to be deflected according to Hooke's law. A laser light is reflected off the back of the cantilever and collected by a detector consisting of two closely spaced photodiodes. When the cantilever is deflected it results in one of photodiodes collecting more light than the other, thus producing an output signal which is proportional to the deflection of the cantilever [67].

In principle, at the tip only one atom should interact with the sample surface, thus the sharpness of the tip is of great importance for the quality of the image produced [68]. The forces involved between the atom on the tip and the sample are the electrostatic and the Van der Waals force. Generally, a feedback mechanism is used to adjust the tip to sample distance to maintain a constant force between tip and sample. This is done so that contact between the tip and the sample is avoided and thus damage to both can be prevented to certain degree [69].

The mode of operation used in these experiments is the tapping mode by which less damage is caused to the tip and the sample than the more conventional contact mode where the tip is gently dragged across the sample [68]. In tapping mode the lever oscillates so that it is not in contact with the sample at all times. The oscillations are keep constant by lifting the tip in the z direction. A schematic of an AFM system is shown in Figure 3.7.

For AFM studies in this report, a p-type Silicone (Si) substrate was cleaned, the substrate was then submerged in acetone and placed in an ultrasonic bath for ~ 10 min then dried. This process was then repeated with methylated spirits and then with Isopropanol. The sample solution was diluted with deionised water in a ratio of 5:1 and placed on the substrate where it was left to dry for ~ 2 min before the excess solution was blown off. The samples were processed in this way to obtain an even distribution of nanocrystals on the substrate.

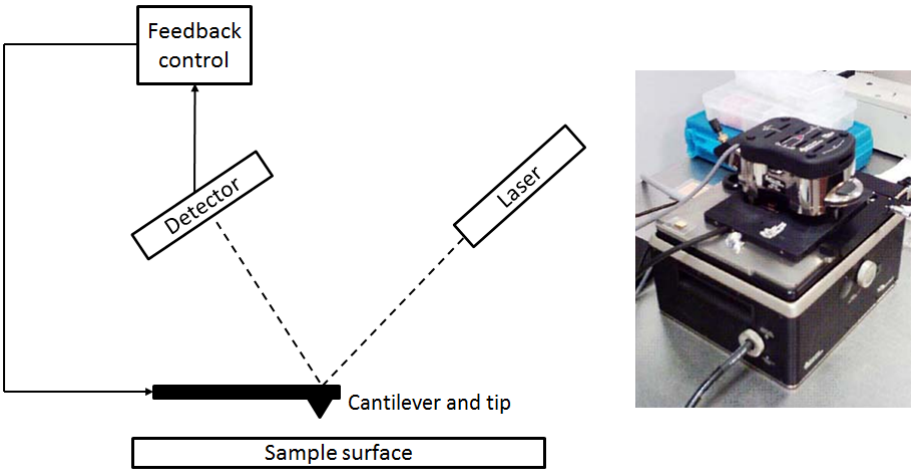

Figure 3.7: Schematic of AFM system and picture of the system used at the University of Nottingham.

3.7 Transmission Electron Microscopy

The transmission electron microscope (TEM) operates using the same basic principles as a visible light microscope, but uses electrons instead of photons. The resolution of a visible light microscope is limited by the wavelength of the photons being used to probe the sample (visible light $400 - 700\,\mathrm{nm}$). Since the de Broglie wavelength of electrons can be much smaller than that of visible light, electrons can be used to obtain resolution approximately one thousand times better. In a TEM, objects can be seen with a resolution in the order of a few angstroms [70]. This vast difference in resolution makes the TEM a valuable tool.

Electrons are charged particles so there are inevitably a few differences in a TEM to a light microscope. The optical system of a TEM must be in vacuum or electrons will interact with charged molecules in the air. Also, as electrons cannot pass through glass, conventional lenses cannot be used in TEM. Therefore magnets are used as lenses and, by changing the strength of the magnetic field, the electron beam can be manipulated and the image can be magnified [71].

Electrons are produced by an electron gun at the top of the microscope. Since electrons cannot be seen by the naked eye as in a visible light microscope, the image is magnified and focused onto an imaging device such as a fluorescent screen or a CCD camera. The sample must be extremely thin for the electrons to pass through and create an image. Sections of the sample must be no more than hundreds of nanometres at the most. Sometimes contrast must be provided by using electron-absorbing heavy metals to stain the samples.

High-resolution TEM (HRTEM) is an imaging mode of the TEM which can produce detailed images of a crystal lattice with atomic resolution. This can provide valuable information on the structure of materials at the atomic scale making it an ideal method for studying nanoparticles. The image is formed by the interference of the direct electron beam and the diffracted beam, this is also known as 'phase contrast' imaging [72].

In this report the nanoparticles were deposited on graphene oxide grids and TEM images were recorded on the JEOL1200EX and JEOL2100F microscopes operating at $120\,\mathrm{kV}$.

Chapter 4

Effects of Mn-doping on the Physical Properties of PbS Nanoparticles

This chapter provides evidence for the successful incorporation of Mn-atoms into PbS nanoparticles, and discusses how this affects their physical properties. This will include how their size, shape, composition, PL and magnetic properties are affected.

4.1 Morphology of the Nanoparticles

Undoped colloidal PbS nanoparticles synthesised by the method described in the previous chapter have an approximately spherical shape and maintain the rock-salt structure of the bulk PbS crystal. The diameter of the QDs produced by this method is tunable in the range $d = 3 - 12\,\mathrm{nm}$ by adjusting the molar ratio of Pb^{2+}/S^{2-} reactants used to form the nanoparticles [53]. In this study the ratios were maintained as described previously to obtain average diameters of $d = 5\,\mathrm{nm}$.

Many of the physical properties of PbS nanoparticles are affected by the incorporation of Mn-atoms. However the size, shape and crystal structure do not seem to be significantly altered. HRTEM images show Mn-doped and undoped PbS nanoparticles of similar sizes with diameters $d \sim 5\,\mathrm{nm}$. Selected area electron diffraction studies also show that the doped nanoparticles maintain the rock-salt structure of the undoped nanoparticles and bulk crystal. Figure 4.1 shows a HRTEM image of a typical $Pb_{1-x}Mn_xS$ nanoparticle and nanoparticle ensemble where $x = 10\,\%$. Crystal planes can also be seen in the HRTEM images. The clearly defined lattice fringes have a spatial separation of $a = 2.7 \pm 0.1\,\text{Å}$ and $a = 3.3 \pm 0.1\,\text{Å}$. These values match well with previous studies of PbS QDs of similar size [73, 74] and the interplanar distances of the (220) and (111) planes of bulk PbS, where $a = 2.73\,\text{Å}$ and $a = 3.42\,\text{Å}$ respectively [73]. This gives further evidence that Mn incorporation does not significantly affect the crystal structure of the nanoparticles.

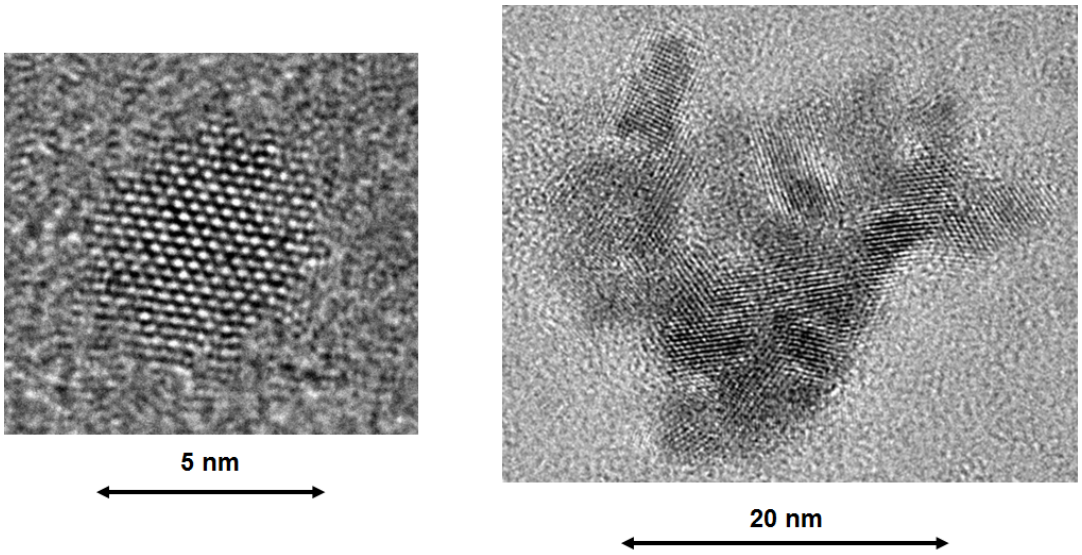

Figure 4.1: HRTEM images of a single $Pb_{1-x}Mn_xS$ nanoparticle (left) and an ensemble of nanoparticles (right) with $x = 10$ %.

Figure 4.2 shows typical AFM images for $Pb_{1-x}Mn_xS$ nanoparticles where $x = 0$ (a) and 10 % (b). The height-profiles and height-histograms show the statistical distributions of height-values within the images. These AFM studies suggest that the size distribution of the QDs is not significantly affected by the Mn-content. For undoped PbS nanoparticles the average height derived from the AFM images is $d = 4.5 \pm 1.0\,\mathrm{nm}$, for $x = 5\,\%$, $d = 4.5 \pm 1.8\,\mathrm{nm}$ and for $x = 10\,\%$, $d = 4.5 \pm 1.5\,\mathrm{nm}$. Although the average size of the QDs is not affected, there is a small increase in the width of the size distribution with the incorporation of Mn-atoms.

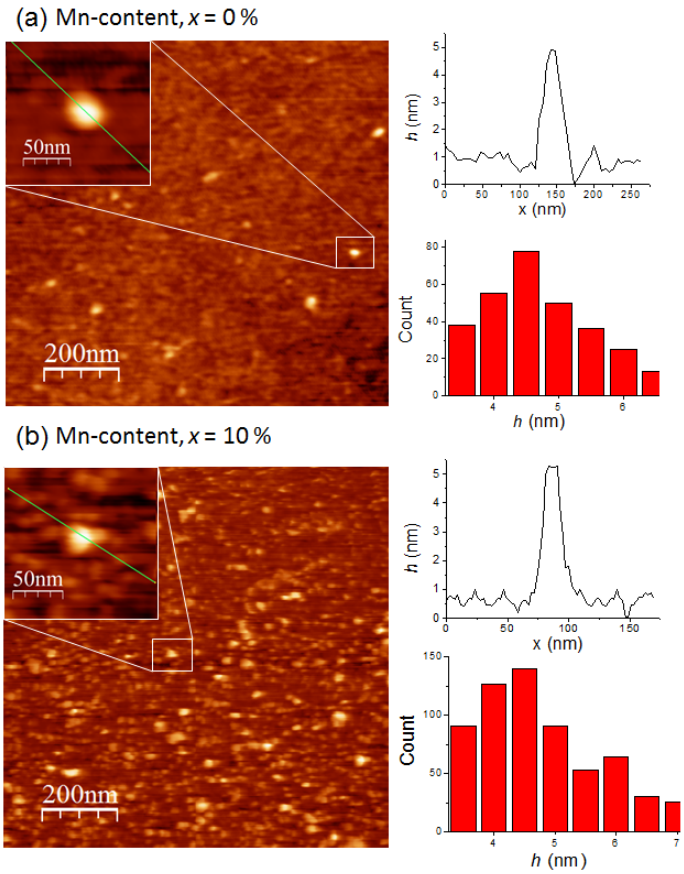

Figure 4.2: Typical AFM images and height (h) profiles for PbS (a) and Mn-doped PbS (b) nanoparticles. The height histograms show the statistical distributions of height-values within the images and indicate that the incorporation of Mn in the PbS nanoparticles does not cause any significant change in the height distribution.

The chemical composition of the nanoparticles is derived from EDX measurements. These show strong evidence for the incorporation of Mn-atoms into PbS QDs. Figure 4.3 shows a typical EDX spectrum for an ensemble of nanoparticles with $x = 10\,\%$. An EDX peak associated with Mn is clearly observed at an energy of 5.9 keV. These measurements also show that the Mn-concentration estimated by EDX, M_{EDX}, is significantly lower than the nominal value x. Therefore only a fraction of Mn used in the solution during synthesis is incorporated into the nanoparticles. This deviation increases with increasing x, as shown in Figure 4.3. For example, for $x = 10\,\%$ EDX measurements show $M_{EDX} = 4\,\%$ corresponding to an average number of Mn-ions per QD of $n_{Mn} = 110$. It is also worth mentioning here that although the EDX measurements verify the presence of Mn, they do not give any information of the valance state or the location of Mn.

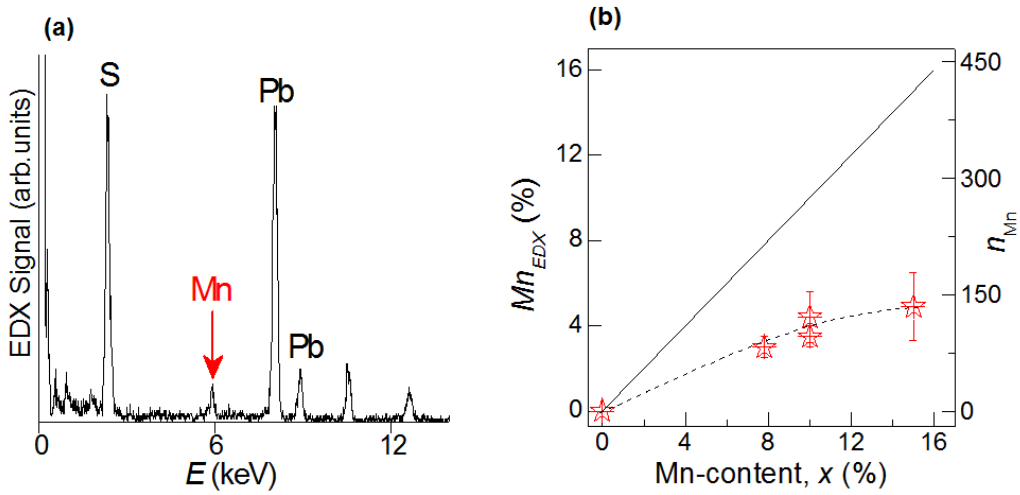

Figure 4.3: EDX spectrum of $Pb_{1-x}Mn_xS$ nanoparticle with x=10 % (a) and Mn-content measured by EDX, M_{EDX}, versus the nominal Mn-content, x (b). The continuous line represents the nominal Mn-content. The dashed line is a guide to the eye. The right axis represents the estimated number of Mn-ions per QD.

Difficulties in achieving high levels of doping in nanocrystals are not uncommon. As mentioned in chapter two, the process of 'self-purification' can be partially responsible for this deviation [8]. Due to the lack of sensitive experimental techniques for locating the dopants in individual nanoparticles, the statistical distribution of the dopant concentration and the size of the individual nanoparticles, it is generally difficult to assess the exact position of the dopants within a nanocrystal and their preferential site within the crystal lattice. The deviation between the nominal and actual amount of Mn incorporated into the nanoparticles is also observed when looking at their PL properties, which will be described in more detail in the next section.

It is also worth mentioning here that the stability of the nanoparticles properties are largely unaffected by the incorporation of Mn and their properties remain stable for at least three months.

4.2 PL Properties

The incorporation of Mn-atoms into PbS nanoparticles has pronounced effects on their PL properties, affecting the peak emission energy, optical linewidth and, to a lesser degree, the intensity of the emission.

Increasing Mn-content has the effect of broadening the optical linewidth, although a clear dependence of the broadening with increasing x is not observed. AFM studies show that there is a small difference in the size distribution, which makes a contribution to the broadening. Other contributions are likely to arise from an increase in the compositional disorder within the QD ensemble, i.e QDs containing different Mn-content.

The PL intensity decreases by less than a factor of 10 going from $x = 0$ to 18 %, thus indicating a low level of thermal escape of carriers from the dots and a relatively low density of Mn-induced non-radiative recombination centres. It is important to make clear that the percentage values given in this chapter refer to the Mn precursor level introduced during synthesis and not to the amount of Mn successfully incorporated into the nanoparticles.

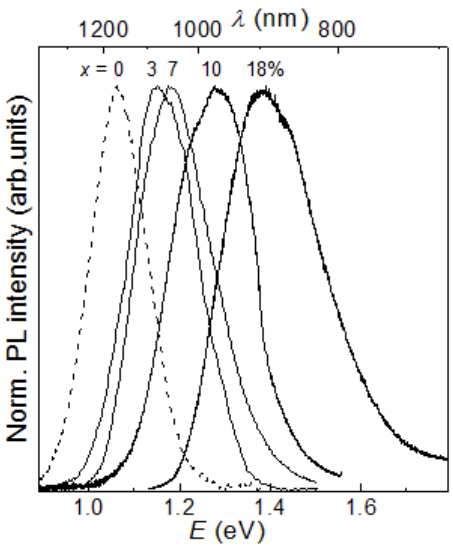

Figure 4.4: Normalised PL spectra of QDs with x from 0 to 18 % at $T = 300$ K and laser excitation wavelength $\lambda = 633$ nm.

With the incorporation of Mn into the nanoparticles, the peak energy of the PL emission blue-shifts. For undoped PbS QDs, $E_{QD} = 1.08\,\mathrm{eV}$ ($\lambda = 1150\,\mathrm{nm}$) at $T = 300\,\mathrm{K}$. Increasing Mn above $x \sim 1\,\%$ results in a gradual energy blue-shift of the PL emission to a value of $E_{QD} = 1.4\,\mathrm{eV}$ ($\lambda = 885\,\mathrm{nm}$) for $x = 18\,\%$, as shown in Figure 4.4.

This Mn-induced energy blue-shift of the QD PL emission can be attributed to an alloy effect. The theoretical values of E_{QD} can be calculated using equations 2.6 and 2.7, where $m^* = 0.09m_e$. To account for different values of E_{QD} at $x = 0$ % in different sets of nanoparticles, in the calculations we have assumed slightly different values of the QD radii in the range $R = 2.5 - 2.6\,\mathrm{nm}$. Figure 4.5 shows that the calculated value of E_{QD} increases almost linearly with increasing x and the measured values fit well at small x.

The different symbols in Figure 4.5 correspond to different sets of samples, i.e. samples that were produced during different syntheses. Red indicates samples that have been synthesised more recently and show that greater control is being achieved during synthesis as the PL properties better agree with the calculated values. The logarithmic scale in Figure 4.5 (b) better highlights the smaller concentrations which are more difficult to distinguish in Figure 4.5 (a). Values of the PL peak position of undoped PbS nanoparticles in Figure 4.5 (b) are plotted at $x = 0.01$ % so they can be seen on the logarithmic scale.

The disagreement at large x is attributed to a partial incorporation of Mn into the nanocrystals as noted before from the EDX studies. The values of the Mn-concentration, $\mathrm{Mn_{PL}}$, derived from the measured and calculated dependence of E_{QD} on x are broadly in line with those of $\mathrm{Mn_{EDX}}$, see Figure 4.6. Thus this analysis indicates an effective Mn-doping level of up to $8\,\%$ for $x = 18\,\%$.

Unlike Mn-doped II-VI nanocrystals [8, 75], the PL emission of the Mn-dopants is either not observed or is much weaker than the QD emission. We find that its energy position does not depend on x. Figure 4.7 shows the weak Mn-related PL band centred at $1.9\,\mathrm{eV}$, which is at higher energies relative to the much stronger PL emission of the nanocrystals centred at ~ 1.2 eV for $x = 7$ %.

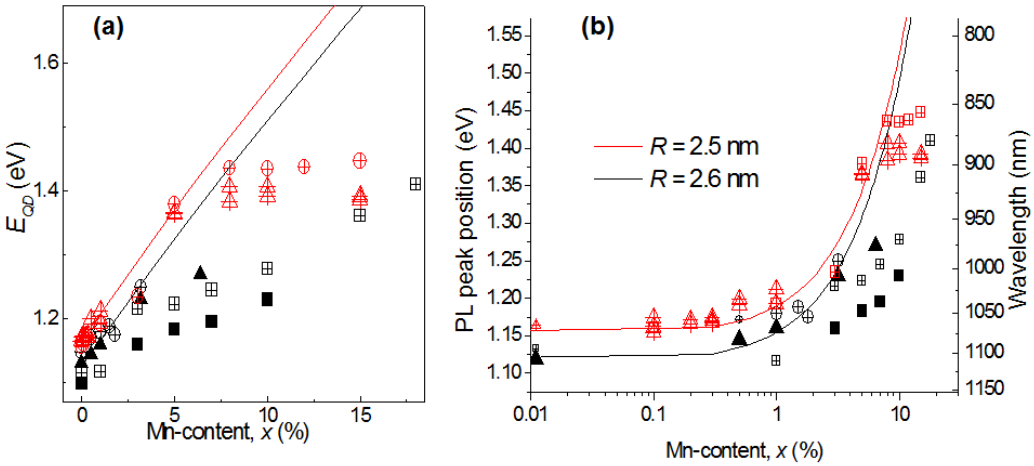

Figure 4.5: Dependence of E_{QD} on x at $T = 300$ K. Different symbols refer to data from QDs from different syntheses. To account for different values at E_{QD} at $x = 0$ % in different sets of nanoparticles, in the calculation of E_{QD} we have assumed slightly different QD radii where $R = 2.5$ nm (red line) and 2.6 nm (black line).

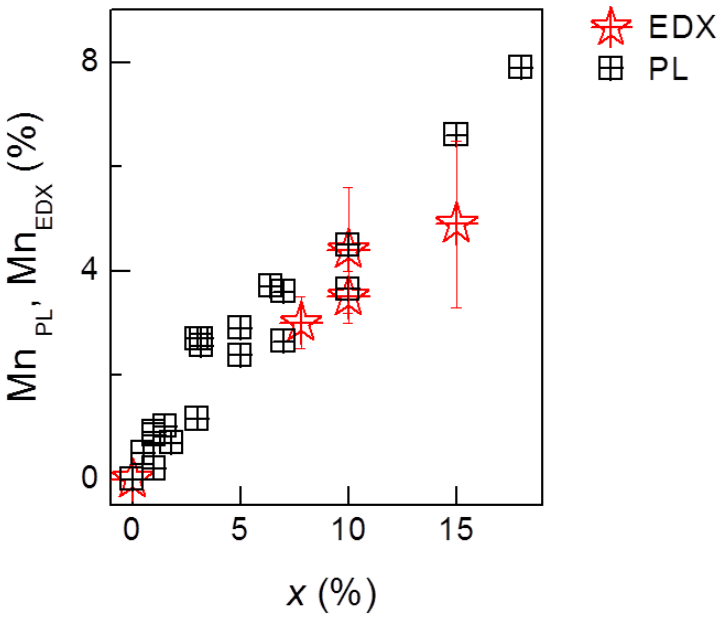

Figure 4.6: Mn-content as estimated from EDX (stars) and from calculated and measured values of E_{QD}. As with Figure 4.5, to account for different values of E_{QD} at $x = 0\,\%$, we have assumed slightly different values of the QD radii.

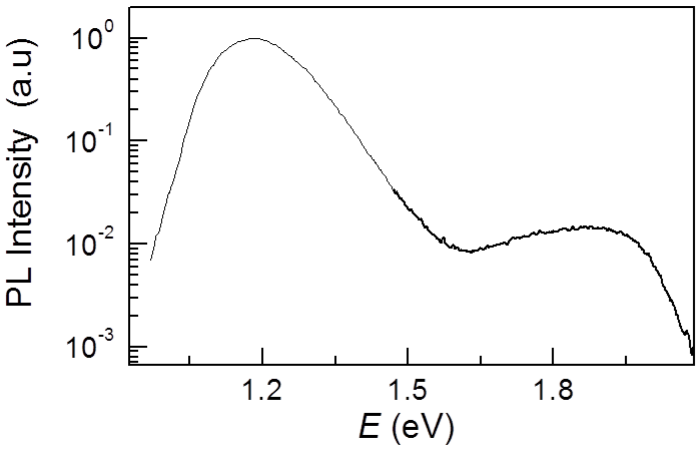

Figure 4.7: PL Spectrum for QDs with $x = 7$ % showing the Mn-dopant PL emission at 1.9 eV and the emission from the QDs at lower energy at $T = 300$ K, laser excitation wavelength $\lambda = 633$ nm and $P = 25$ W/cm^2.

4.3 Temperature Dependence of PL Properties

For temperatures ranging from 3.5 K to 300 K, the PL properties of both Mn-doped and undoped PbS QDs are significantly affected. For both there is a significant quenching of the PL intensity as the temperature increases. This property is not significantly affected by the Mn-content. The optical linewidth broadens for both as the temperature increases and the incorporation of Mn-atoms does affect the way the linewidth depends on temperature. The most interesting change in the temperature dependent PL properties due to Mn incorporation is that of the PL peak energy shift. This section will describe the changes in all temperature dependent PL properties due to Mn incorporation with a focus on the PL peak energy shift.

Figures 4.8 and 4.9 show examples of typical PL spectra for undoped PbS nanocrystals and $Pb_{1-x}Mn_xS$ nanocrystals ($x = 8$ %) respectively, and show how their PL properties are affected by temperature in the range 3.5 to 300 K. The two figures show some significant differences in the dependence of the PL properties with temperature.

For both doped and undoped samples, an increase in T from 3.5 to 300 K decreases the intensity by less than factor of 10. The quenching of the PL intensity as the temperature increases is attributed to the activation of non-radiative re-

combination processes. As seen in Figure 4.8, for PbS nanocrystals the intensity reaches a maximum at $T \sim 50$ K and thereafter decreases. This behaviour has been reported in previous studies of these PbS QDs [50, 53]. It has been attributed to the thermally activated redistribution of carriers in the QD in the presence of defects, whereby carriers that are trapped in defect sites overcome the energy barrier and fall into the QD ground state [53]. For samples with $x > 1$ %, the peak intensity does not reach a maximum at 50 K but at 3.5 K, see Figure 4.9. This suggests that the incorporation of Mn tends to increase the number of non-radiative recombination centres.

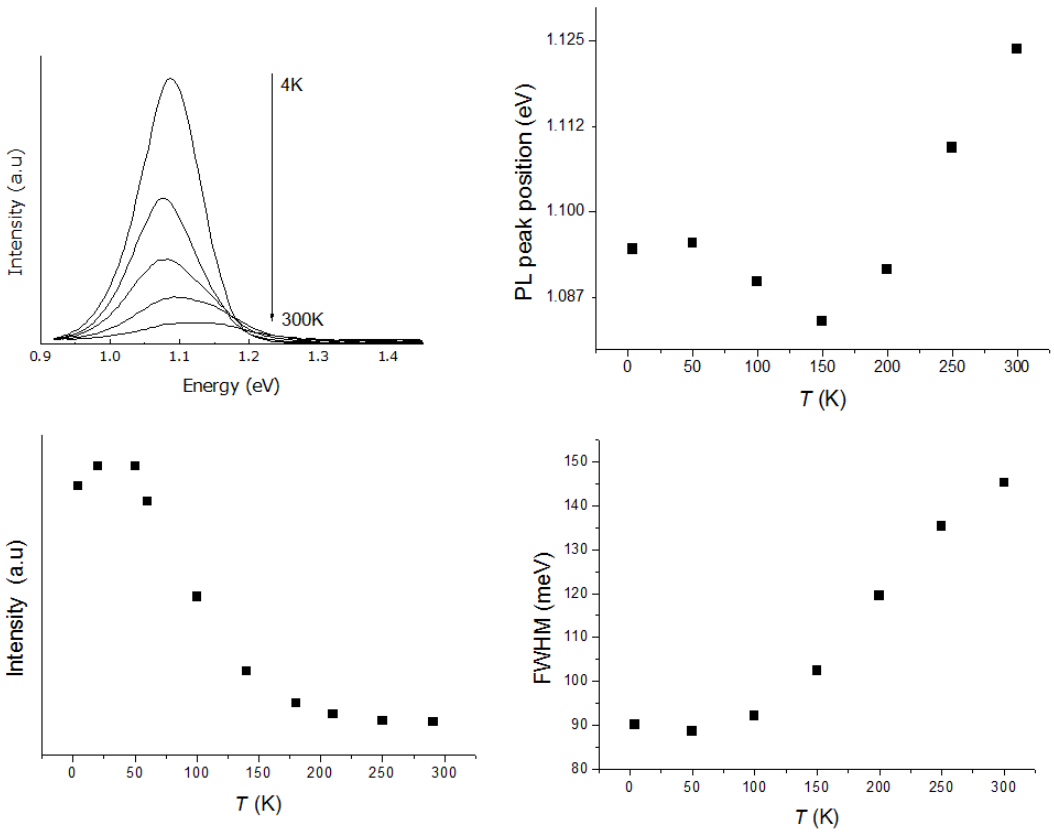

Figure 4.8: Temperature dependence of the PL properties for PbS nanoparticles showing the PL peak energy, the Full-Width at Half Maxima (FWHM) and the PL intensity ($\lambda = 633$ nm and $P = 25$ W/cm^2).

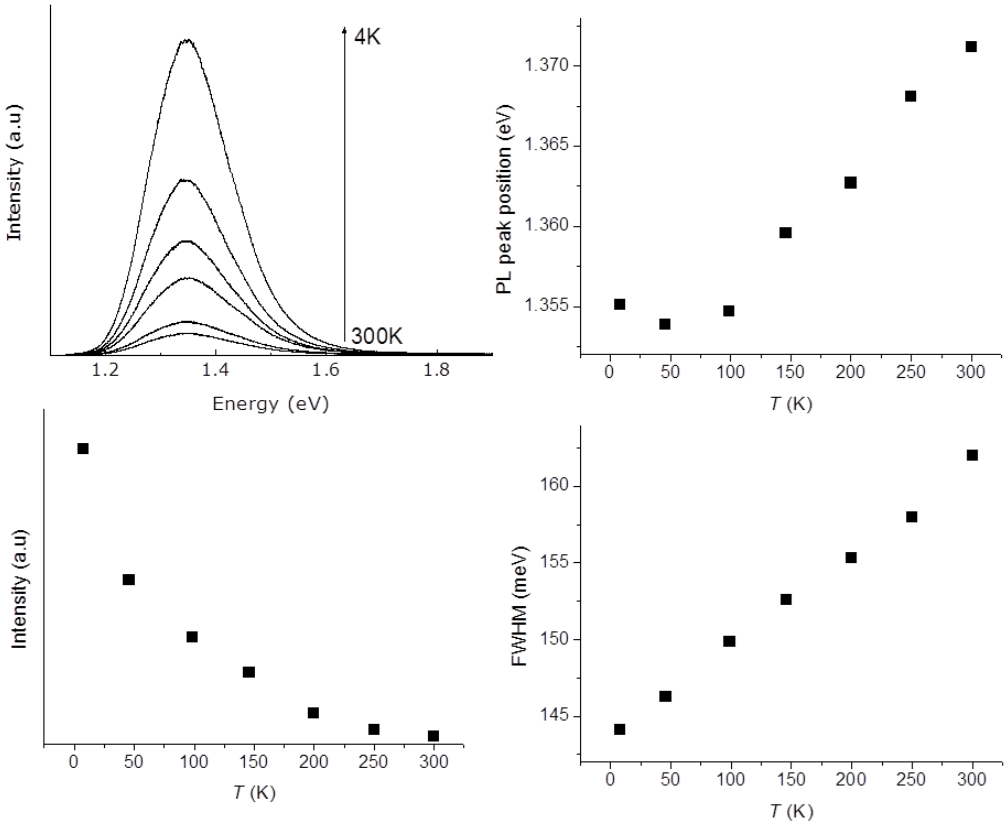

Figure 4.9: Temperature dependence of the PL properties for $Pb_{1-x}Mn_xS$ nanoparticles with $x = 8\,\%$ showing the PL peak energy, the FWHM and the PL intensity ($\lambda = 633$ nm and $P = 25$ W/cm^2).

The optical linewidth of the PL signal is also T-dependent and significantly broadens with increasing temperature for both doped and undoped PbS QDs . Carriers in QDs, unlike isolated atoms, couple to the vibrational modes of the crystal lattice. Charges localised in the nanoparticle interact with lattice vibrations via phonons. This electron-phonon interaction leads to a homogeneous broadening of the optical linewidth with increasing temperature [76]. The PL linewidth is also controlled by an inhomogeneous broadening due to the size/shape distribution of the QDs and spectral diffusion due to charge trapping on dot defects [77]. Previous studies of PbS nanoparticles show thermally activated broadening of the linewidth at $T \sim 100$ K [53]. This thermal activation is also observed for undoped PbS nanoparticles in this study (Figure 4.8) and indicates that at high T the optical linewidth is also controlled by an intrinsic scattering process due to carrier interaction with phonons. Specifically the broadening is explained in terms of the dephasing of the electronic states by interactions with longitudinal optical phonons [53].

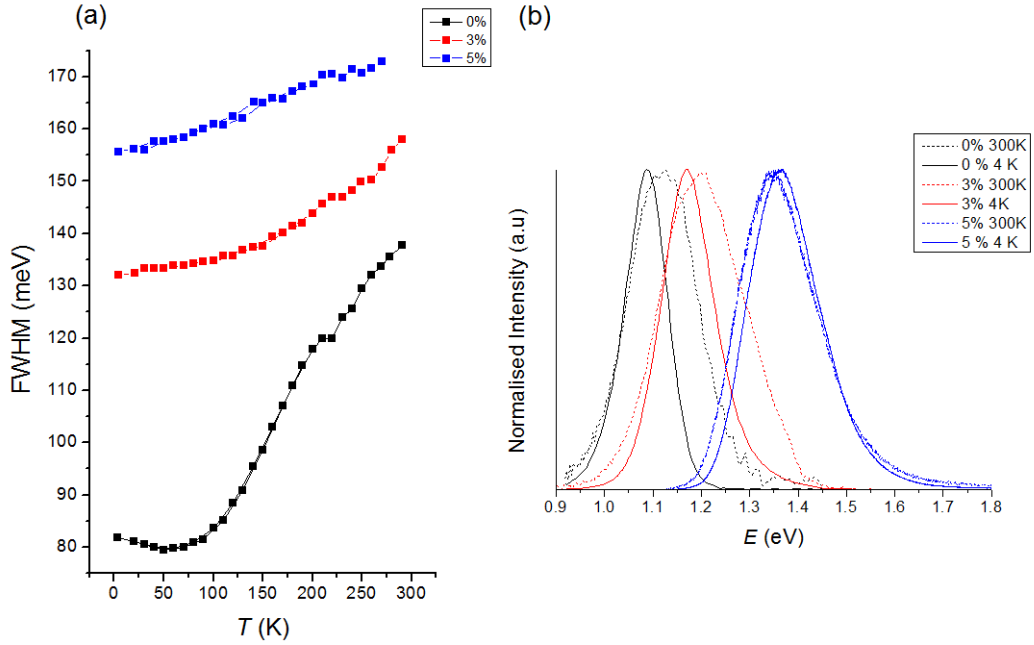

Figure 4.10: (a) Temperature dependence of the FWHM for $Pb_{1-x}Mn_xS$ nanoparticles with Mn-content, $x = 0$, 3 and 5 % and (b) corresponding PL spectra at 3.5 and 300 K ($\lambda = 633$ nm).

The incorporation of Mn into the nanocrystals significantly affects the thermal activation of the linewidth broadening. For samples where $x \geq 5$ %, no thermal activation of the linewidth broadening is observed and the broadening becomes linear with increasing temperature. Figure 4.10a shows how the increasing Mn-content affects the linewidth dependence on temperature for $x = 0$, 3 and 5 %. The corresponding PL spectra at 3.5 K and 300 K are shown in Figure 4.10b.

These observations indicate that the increased inhomogeneity due to Mn incorporation gives rise to more complex carrier-phonon interaction mechanisms than those that were previously used to describe the thermally activated linewidth broadening in PbS QDs.

The property that is affected which is of the most interest for this study is that of the PL peak energy. There are several mechanisms that can account for the shift in PL energy due to temperature changes. These include contributions from electron-phonon coupling [78] and the thermal expansion of the crystal lattice [78]. There are also other mechanisms that contribute in QDs due to the nanoparticles size

such as strain between the thermal expansion mismatch between the nanoparticle and its capping layer [79] and thermal expansion of the wave-function envelope whereby as a QD undergoes thermal expansion, the quantum confined energy levels shift [79]. These complex mechanisms can lead to a red-shift or blue-shift in the PL peak energy depending on the materials involved.

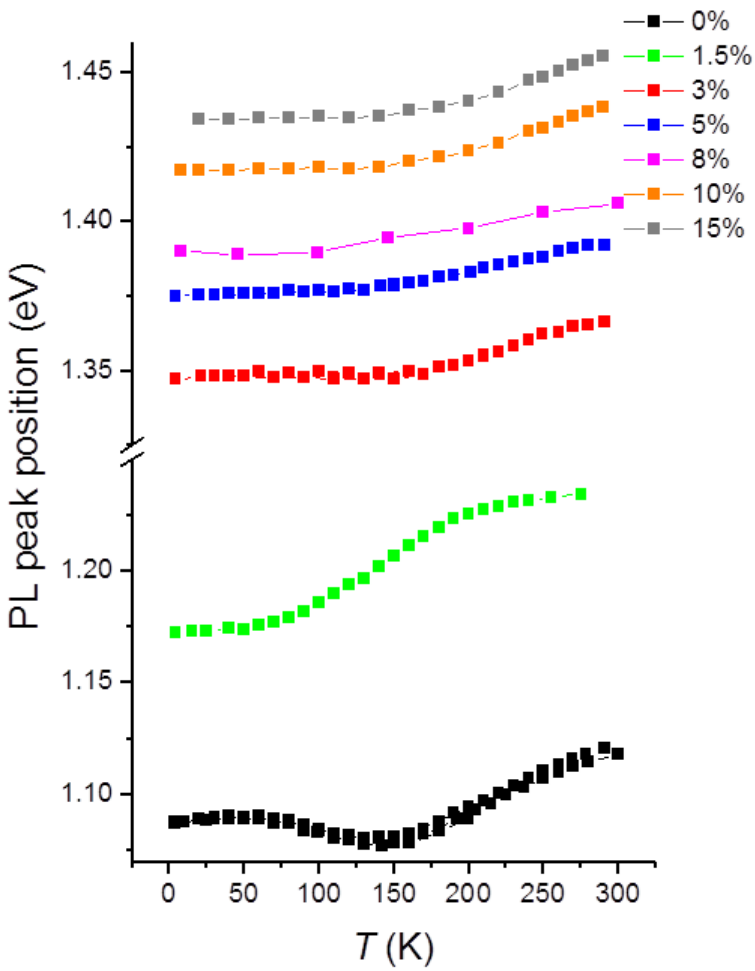

Figure 4.11: Temperature dependence of PL peak position of $Pb_{1-x}Mn_xS$ nanoparticles with x up to 15 % ($\lambda = 633$ nm).

Figure 4.11 shows the T-dependence of the PL peak energy for $x = 0$ to 15 %. The energy shift in the PL peak provides further evidence for the formation of alloyed nanocrystals. For PbS QDs and those containing Mn, we observe an energy blue-

shift of the PL band that is approximately linear at $T > 150\,\mathrm{K}$. Over this temperature range we observe a decrease in the temperature coefficient $dE_{QD}/dT = \alpha_{QD}$ with increasing Mn. This decrease is what we would expect for alloyed (PbMn)S nanoparticles, as it is positive for bulk PbS (α^{PbS}=+0.52 meV/K) [12], but negative for MnS ($\alpha^{MnS} = -2\,\mathrm{meV/K}$) [14]. For undoped PbS QDs, $\alpha = 0.27\,\mathrm{meV/K}$, which is similar to the value reported for PbS QDs of similar size [30, 53, 80]. For samples incorporating Mn (when $x > 1\,\%$), the coefficient tends to become significantly smaller, e.g. 0.12 meV/K for $x = 7\,\%$.

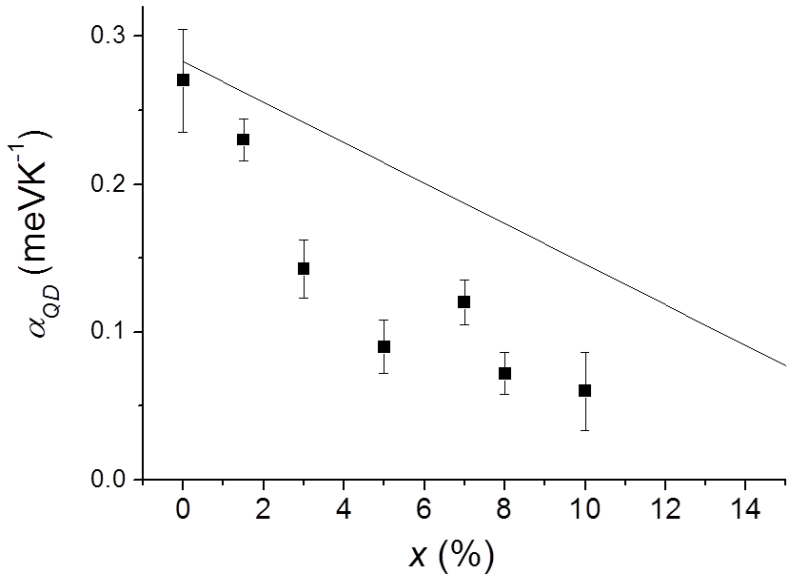

Figure 4.12: Calculated and experimental values of the temperature coefficient $\alpha_{QD} = dE_{QD}/dT$.

As described in chapter two, Vegard's law and the calculated values of E_{QD} on x (equation 2.8) can be used to calculate α_{QD}. Figure 4.12 shows that the experimental values and the calculated values of α_{QD} show a similar dependence of α_{QD} on x. The deviation in the theory and experiment is not completely unexpected as the theory does not take into account the increased inhomogeneity of the samples and the presence of an oxide layer surrounding the nanoparticles, which will be discussed later.

These observations and those in the previous section do not depend on the laser excitation power used in the PL studies, which was varied over a wide range in all experiments. Figure 4.13 shows that the laser power, in the range $P = 0.1 - 10$ W/cm^2, does not effect temperature dependent PL properties for PbS

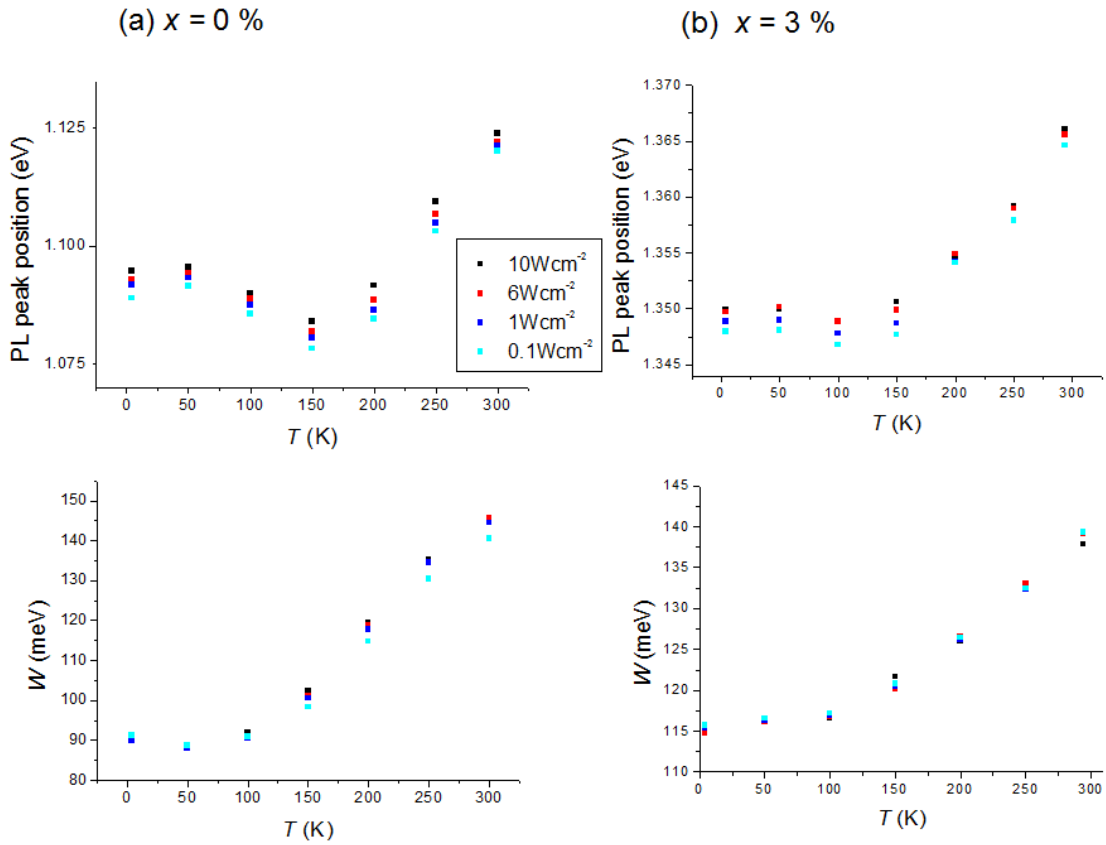

Figure 4.13: Effect of laser power on temperature dependent PL properties for $x = 0$ % (a) and $x = 3$ % (b).

nanoparticles and nanoparticles where $x = 3$ %. However note that we observe a blue-shift of the PL peak energy with increasing laser power which is likely to be caused by a band filling effect [81].

4.4 Magnetic Properties

EPR measurements show evidence that $Pb_{1-x}Mn_xS$ nanoparticles are paramagnetic. Figure 4.14a shows the room temperature K-band EPR spectra of Mn-doped PbS nanoparticles with x up to 5 %. For $x = 0.5$ %, the EPR spectrum shows six narrow resonances superimposed on a broad background signal. These six lines are due to magnetic resonance transitions between states that are split by the hyperfine interaction between d-shell electrons ($S = 5/2$) and the nuclear spins ($I = 5/2$) of the Mn^{2+} ions. With increasing Mn-content, the six resonances be-

come broader until they merge into a single broad lineshape for $x = 5\,\%$. This broadening is ascribed to an increasing Mn-Mn dipolar interaction. The simulation of the broad EPR spectra using a single Lorentzian lineshape indicates a hyperfine splitting constant $A = 9.25\,\mathrm{mT}$ and a g-factor value of ~ 2, which is similar to those reported before for PbS nanoparticles in a glass matrix [82].

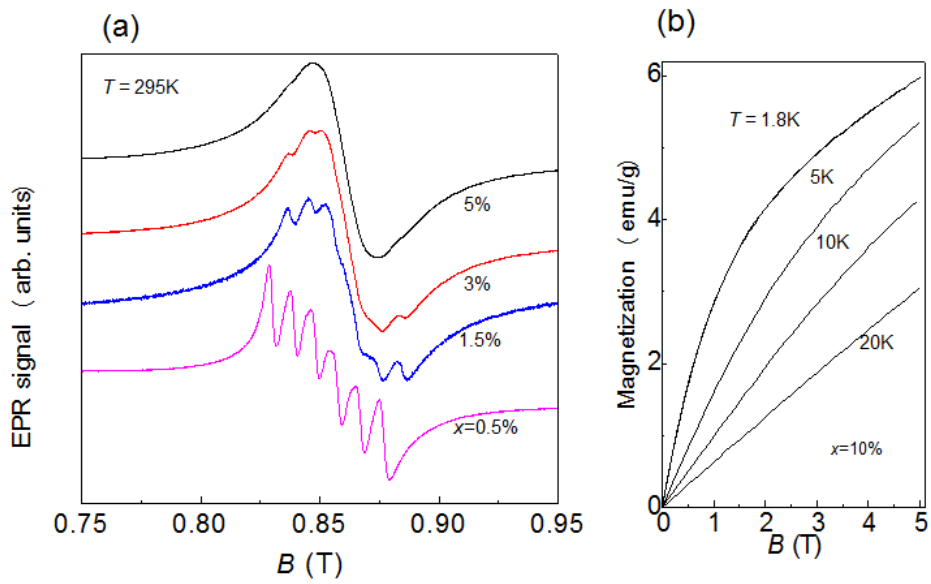

Figure 4.14: EPR measurements (a) and SQUID measurements (b) for $Pb_{1-x}Mn_xS$ nanoparticles.

The asymmetric shape of the EPR lines in Figure 4.14a indicates an additional unresolved hyperfine splitting due to the contribution from Mn-ions on the surface and in the core of the nanoparticles. As mentioned previously, nanoparticles have a tendency to 'self purify' so we would expect to see some Mn-atoms occupying the preferred Pb lattice site and some on the surface of the nanocrystal.

SQUID measurements (shown in Figure 4.14b) confirm that the Mn-doped PbS quantum dots are paramagnetic: for $x = 10\,\%$, the magnetization tends to saturate for $B > 3\,\mathrm{T}$ to a value of $6\,\mathrm{emu/g}$ at $T = 1.8\,\mathrm{K}$ that decreases with increasing T. This value is about 10-times larger than that reported for PbS QDs in organic solution with $x = 3\,\%$ ($0.5\,\mathrm{emu/g}$) [40].

Chapter 5

Photoinduced Phenomena in $Pb_{1-x}Mn_xS$ Nanoparticles

There are a number of interesting phenomena induced by light in $Pb_{1-x}Mn_xS$ nanoparticles; these include changes in the PL peak emission energy, an enhancement of the PL intensity, a quenching of the intensity of the Mn-related emission and the appearance of Raman peaks. Laser light and long exposure times were required to induce the phenomena described in this chapter.

5.1 Photoinduced changes in the PL properties

To study the effect of light on the PL properties of $Pb_{1-x}Mn_xS$ nanoparticles, the nanoparticles were drop-cast on a glass substrate and exposed to laser light for a time $t_L = 30-120$ min. The excitation power, P, was varied with power densities of 25 W/cm^2, 100 W/cm^2 and 1000 W/cm^2.

5.1.1 Blue-shift of the PL Peak Energy

In all samples containing Mn, the PL emission blue-shifts with increasing t_L. A saturation in the blue-shift ($\Delta E_{QD} = 5-30$ meV) is observed after a characteristic

time t_L^* that depends on the excitation power. Typical PL spectra and correspondingly dependences of the PL peak energy versus time are shown in Figure 5.1 for a sample with $x = 1$ %. As can be seen in the figure, laser excitation also has a significant effect on the PL intensity. This section will focus on the blue-shift of the PL emission and the following section will focus on the PL intensity enhancement.

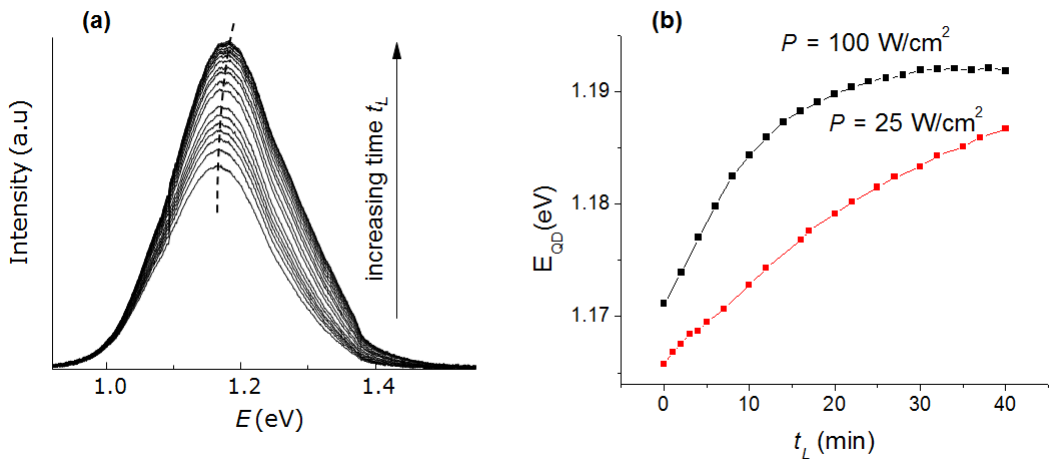

Figure 5.1: (a) Typical room temperature spectra for a sample with $x = 1$ % exposed to laser of power $P = 25$ W/cm^2 and time t_L up to 40 min. The dotted line is a guide to the eye and illustrates the shift of the PL peak energy with time. (b) Dependence of the PL peak energy E_{QD} on t_L for $P = 25$ and 100 W/cm^2 ($\lambda = 633$ nm).

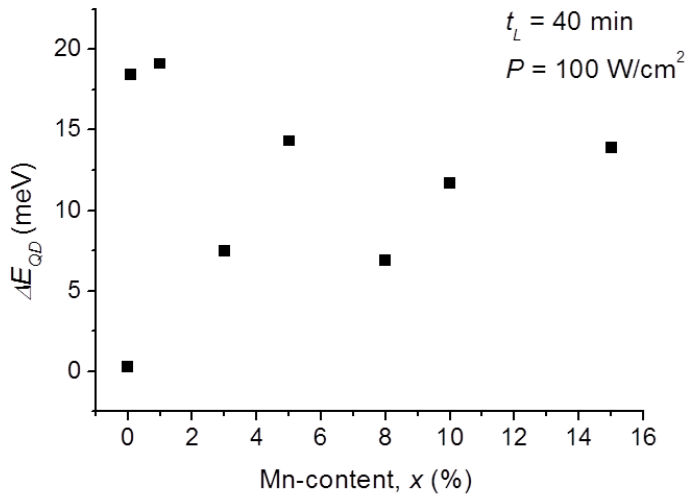

Figure 5.2: Dependence of the energy shift, ΔE_{QD}, on Mn-content after 40 min of continuous irradiation ($P = 100$ W/cm^2, $\lambda = 633$ nm and $T = 300$ K).

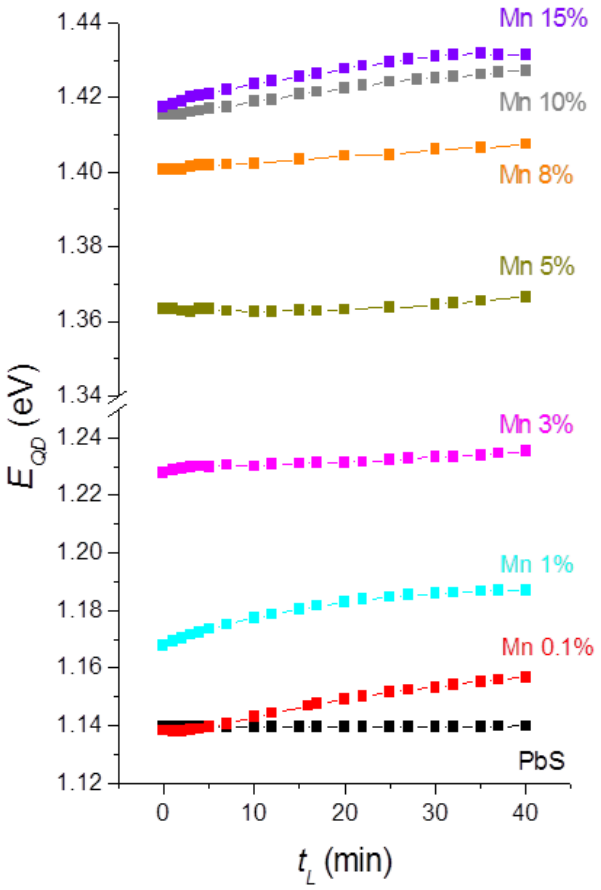

Figure 5.3: Photoinduced blue-shift of the PL peak energy in $Pb_{1-x}Mn_xS$ for $x = 0 - 15$ % ($\lambda = 633$ nm, $P = 25$ W/cm^2 and $T = 300$ K).

Although a blue-shift is not observed in undoped PbS nanoparticles, a systematic dependence of the shift on the Mn-content cannot be identified (see Figure 5.2). Figure 5.3 shows the photoinduced PL peak energy shift over 40 min and $P = 25$ W/cm^2, for $x = 0 - 15$ %.

The effects that the environment has on the photoinduced blue-shift on the PL emission are shown in Figure 5.4. Figures 5.4a and 5.4b show the PL spectra versus time for $Pb_{1-x}Mn_xS$ nanoparticles ($x = 10$ %) in air and in vacuum, respectively. The shifts in time of the PL peak energy are shown in Figure 5.4c. As can be clearly seen in 5.4c, there is no blue-shift when the sample is kept in vacuum and a significant blue-shift (up to 30 meV) in air.

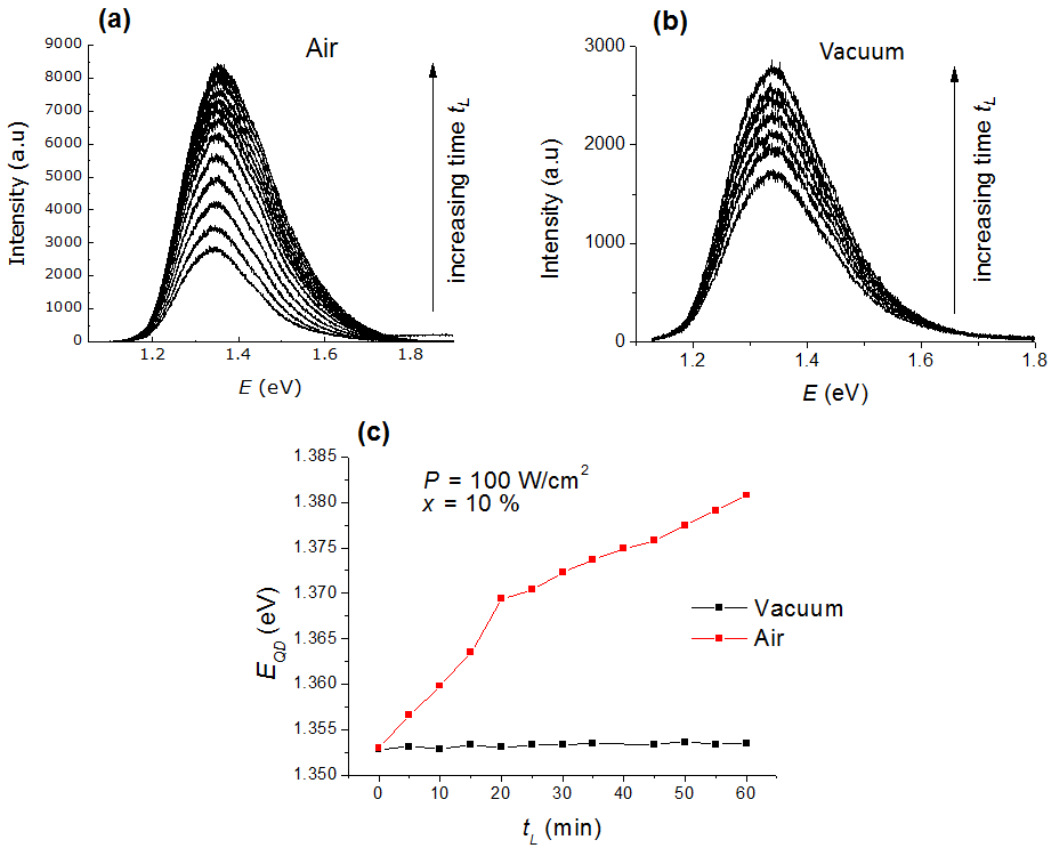

Figure 5.4: Effect of oxygen-containing and oxygen-free environments on the photoinduced PL peak energy shift for $x = 10$ %. PL spectra over 60 min in (a) air and (b) vacuum. E_{QD} versus time for both environments (c) ($\lambda = 633$ nm, $P = 100$ W/cm^2 and $T = 300$ K).

A blue-shift in the PL peak energy could be associated with a reduction in the effective size of the nanoparticles. As the effective size of the nanoparticle reduces, the confinement effects become stronger and thus an increase in emission energy is observed. Mechanisms that have been previously reported to cause a reduction in the effective size of nanoparticles are the chemical etching of the capping ligands, reported in IV-VI colloidal nanoparticles [83]. More widely reported is the photo-oxidation of the nanoparticle surface in CdSe and CdSe/ZnS (core/shell) QDs [84, 85] and PbS QDs [86]. Photooxidation has been confirmed in PbS nanoparticles with power densities down to 30 W/cm^2 by Raman spectroscopy [87]. Our observations on the effect of the environment on the blue-shift allow us to attribute it to the photo-oxidation of the nanoparticles surface as no blue-shift is seen when the experiment is conducted under vacuum. We can also discount the possibility of contributions from chemical ligand etching as this would result in a reduction of

the effective size of the nanoparticle and subsequent blue-shift in both vacuum and air. The observation that the PL peak energy shift saturates quicker for higher powers give further evidence of photo-oxidation. With a greater intensity of light the oxide layer forms faster and thus the peak energy shift saturates more quickly.

As mentioned previously, a significant blue-shift in the PL peak energy is not seen in undoped PbS QDs. The increased instability of the nanoparticle surface and an increase in the number of dangling bonds due to Mn-atoms migrating to the surface of the doped nanoparticles will make them more susceptible to oxidation and may account for why a significant photo-oxidation only occurs for doped nanoparticles. In previous reports of photo-oxidation in undoped colloidal PbS nanoparticles [87], the QDs differ from ours since they have an oleate capping and an average diameter of ∼2 nm. The PbS QDs used in this study appear more stable and thus less susceptible to photo-oxidation as no photoinduced blue-shift in the peak energy is observed.

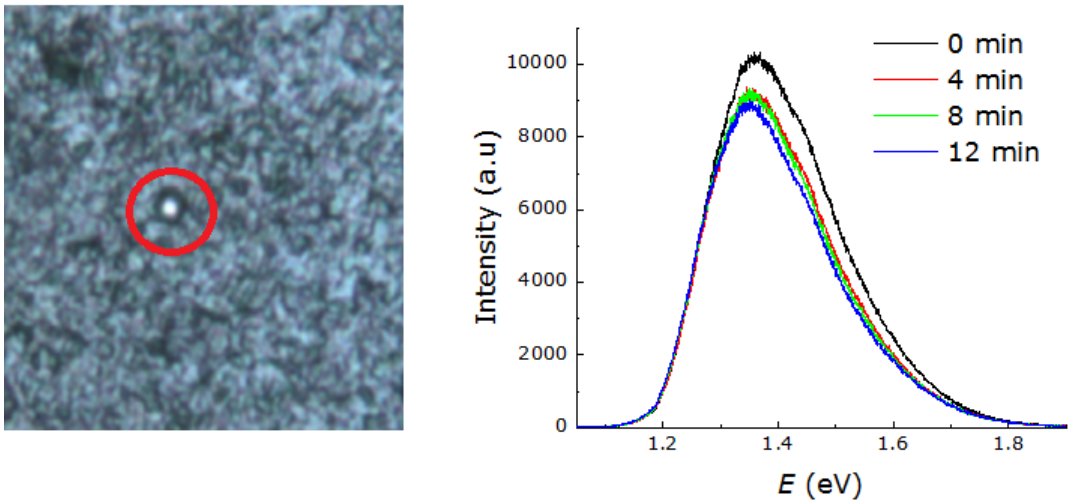

Figure 5.5: Optical image and corresponding of $Pb_{1-x}Mn_xS$ nanoparticle film where $x = 10$ % exposed to laser power density $P = 1000$ W/cm^2 for a time $t_L = 12$ min. The change in the morphology of the nanoparticle film can be clearly seen within the area highlighted by the red circle.

It is also worth noting here that at high laser power densities (≥ 1000 W/cm^2) damage can be clearly seen on the optical images of the samples (see Figure 5.5), thus indicating a macroscopic change in the morphology of the nanoparticle film. This damage is accompanied by a red-shift of the PL peak energy, which can be

attributed to an increase of the QD diameter due to a heating effect. Heating can cause Ostwald ripening whereby larger dots grow at the expense of smaller ones with the smaller dots gradually disappearing, thus leading to an overall increase in the dot diameter [50].

5.1.2 Photoenhancement of the PL Intensity

The photoenhancement of the PL intensity is observed for all samples ($x = 0 - 15$ %) when exposed to continuous irradiation with $P \leq 100$ W/cm^2. The higher the power the quicker this enhancement tends to saturate versus time. At powers of 1000 W/cm^2, damage can be clearly seen in the optical images of the samples. This damage is accompanied by a significant decrease in the PL intensity. This decrease can also be attributed to a heating effect which promotes Ostwald ripening: as the smaller QDs disappear in favour of larger QDs, the overall number of dots that contribute to the PL emission decreases, thus reducing the PL intensity [50].

The enhancement is greater for samples containing Mn than the undoped samples but, as with the PL peak energy shift, a clear dependence on the Mn-content cannot be identified. The lower the power, the greater the enhancement tends to be. The PL intensity can be increased by a factor of $7 - 10$ for $P = 25$ W/cm^2 compared to an increase of $2 - 5$ for $P = 100$ W/cm^2. Also, at the lowest powers ($P = 25$ W/cm^2), the enhancement does not always saturate after 120 min of continuous irradiation.

Figure 5.6a shows the PL enhancement for $x = 0 - 15$ % at $P = 25$ W/cm^2 over 40 min of continuous irradiation. Figure 5.6b shows the spectra for $x = 5$ % over 120 min of continuous irradiation. As can be seen, the intensity enhancement does not saturate after this time period.

Figure 5.7a shows how the photoinduced PL intensity enhancement is effected by the environment. Measurements were taken over 60 min for $x = 10$ % at $P = 100$ W/cm^2 in air and in vacuum (corresponding spectra can be seen in Figure 5.4). The photoinduced PL intensity enhancement is greatly reduced when the sample is in an oxygen-free environment (black) when compared with measurements taken in an oxygen-containing environment (red). In Figure 5.7b measurements were taken

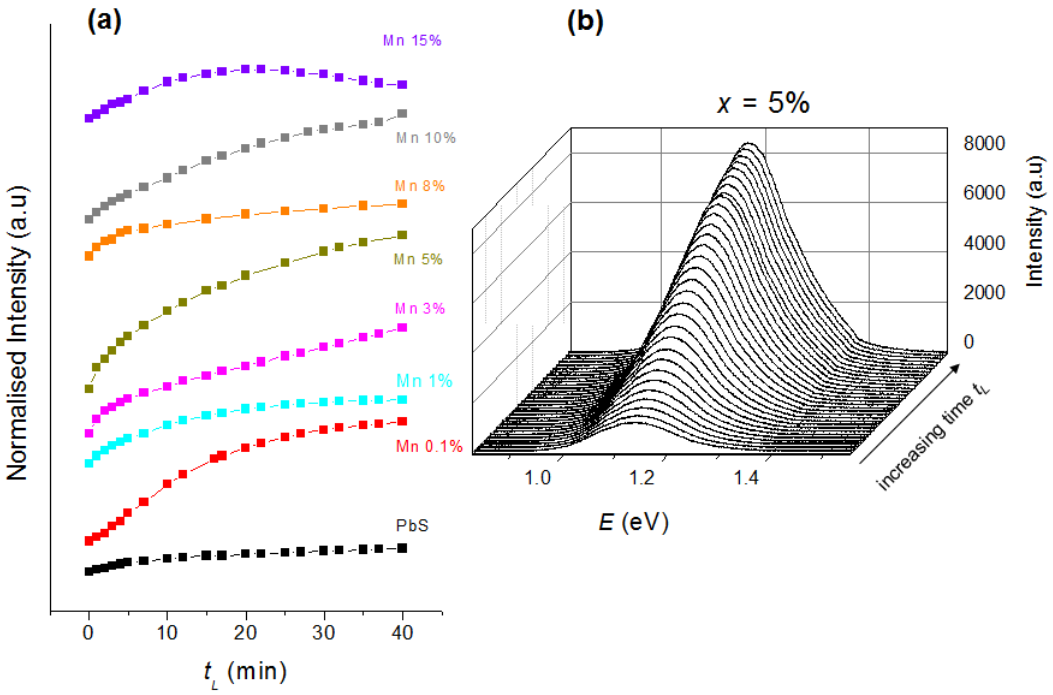

Figure 5.6: (a) PL intensity versus time t_L in $Pb_{1-x}Mn_xS$ nanoparticles for $x = 0$ - 15 %. The data is normalised to the value at $t_L = 0$. For clarity data for different samples are displaced vertically. (b) PL spectra for x =5 % versus exposure time ($\lambda = 633$ nm, $P = 25$ W/cm^2 and $T = 300$ K).

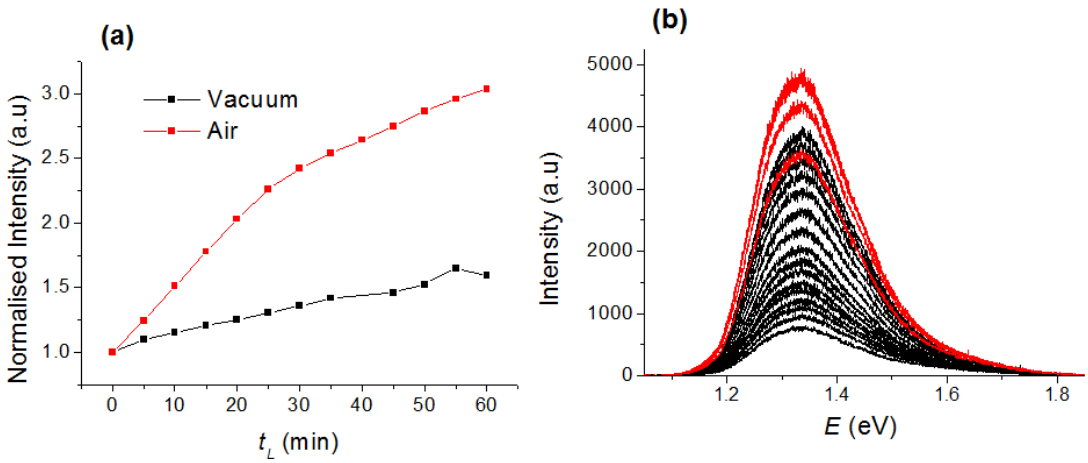

Figure 5.7: (a) Photoinduced PL intensity enhancement in vacuum and in air. The data are normalised to the value at $t_L = 0$. (b) PL spectra at various times. Measurements were taken over 60 min (black), then the sample was left in the dark for 60 min, before measurements were resumed (red) ($x = 10$ %, $\lambda = 633$ nm, $P = 100$ W/cm^2 and $T = 300$ K).

over 60 min (black). Then the samples was left for one hour in darkness before measurements were continued (red). After being left in the dark for one hour, there is a small reduction of ~ 9 % of the intensity. The intensity enhancement continues when the sample is re-irradiated. Previous reports have observed reversibility in the PL intensity enhancement [88, 89] with a reduction of ~ 26 % reported for CdSe QDs under similar experimental conditions [85].

There are a number of mechanisms for the photoenhancement of the PL intensity in QDs that have been previously reported: (1) the passivation of surface defects by surface absorption of water molecules [90]; (2) stabilization of surface traps due to photoinduced ligand rearrangement [85]; (3) photoinjection of carriers to the substrate has been suggested to be the origin of photoactivation [91]; (4) thermal annealing from local laser heating [88] whereby with increasing T, carriers trapped in a defect overcome energy barriers and fall into the ground state of the dot thus increasing the PL intensity; and (5) photo-oxidation can have the effect of reducing surface defects by making a more uniform surface below the oxide layer thus increasing the PL intensity [86]. However, it is also reported in the literature that photo-oxidation can have the effect of quenching the PL intensity as the number of trap sites increases [85].

There are most likely a number of competing processes occurring to produce the observed PL intensity enhancement. However, a major contribution can be attributed to photo-oxidation. This is supported by the large reduction in enhancement under vacuum. The oxidation process is irreversible so observations of only a small reduction after the sample is left in the dark also would agree with an oxidation process. We are also aware that an oxidation process is taking place from observations of the PL peak energy blue-shift described in the previous section.

Since no photoinduced blue-shift is observed in the undoped PbS QDs, we would not expect to see an enhancement of the PL intensity from photo-oxidation. The small photoenhancement that we do observe will be due to the processes which are also be responsible for the photoenhancement of the PL intensity in the Mn-doped QDs when under vacuum. The exact nature of these mechanisms are difficult to determine from our results and are likely be a combination of those reported in the literature and described in preceding paragraphs.

It is also worth noting here that lighting in the laboratory did not have any effect

on the nanoparticle PL properties. Also, the observations of the PL peak energy shift and the photoenhancement of the PL intensity do not have any dependence on laser excitation wavelengths of $\lambda = 633$ nm and $\lambda = 532$ nm.

5.1.3 Photoinduced Quenching of the Mn-related PL Emission

Freshly synthesised doped PbS nanoparticles with $x > 5$ % exhibit a Mn-related PL emission at 1.9 eV (600 nm), which is much stronger than that previously reported in the preceding chapter. With samples that are left in the dark for 2 - 3 weeks after synthesis, the intensity of this band is reduced and samples exhibit the weak band previously described. This band has been previously reported in Mn doped II-VI systems, where the emission occurs at energies smaller than the QD emission [8, 35]. This has been attributed to an internal Mn transition.

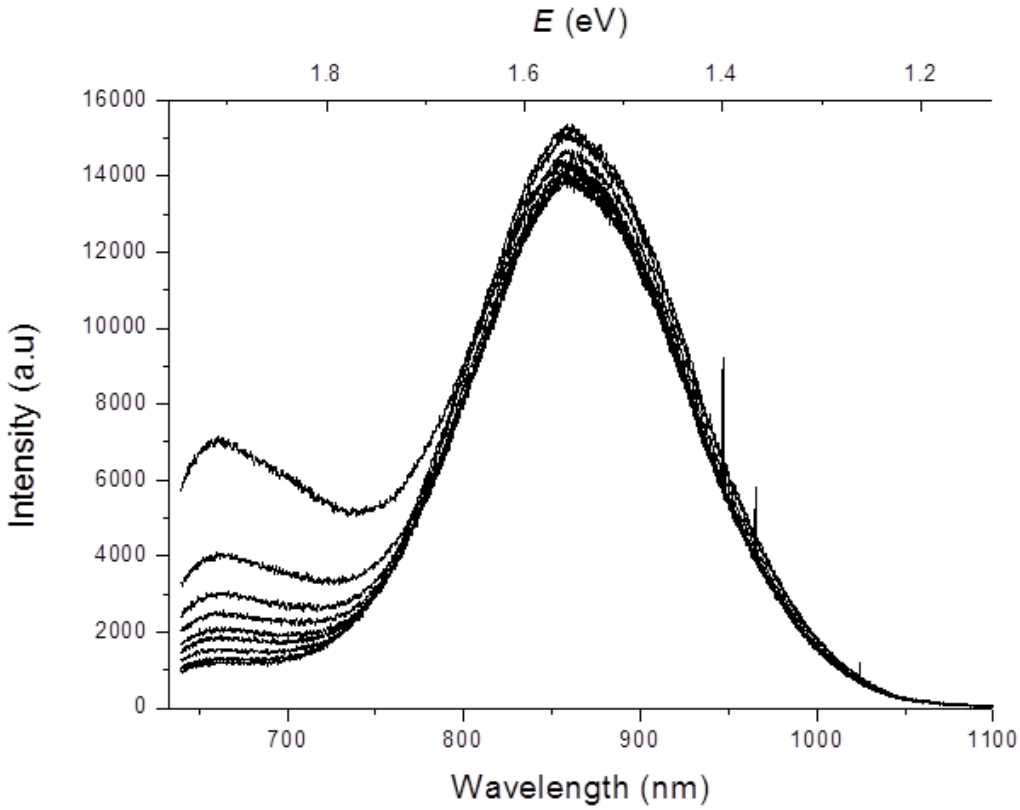

Figure 5.8: Photoinduced reduction of the Mn-related emission for doped $Pb_{1-x}Mn_xS$ nanoparticles with $x = 12$ % over 12 min ($\lambda = 633$ nm, $P = 100$ W/cm^2 and $T = 300$ K).

In freshly synthesised samples, the Mn-related emission quickly quenches under continuous illumination. After $\sim$ 15 minutes the band reaches intensity levels comparable to those described in the previous chapter or disappears completely. Figure 5.8 shows the quenching for the Mn-related band due to continuous illumination for $x = 12$ % with an excitation wavelength $\lambda = 633$ nm, $P = 100$ W/cm^2 over 12 min at $T = 300$ K. The sample in Figure 5.8 was measured one day after synthesis.

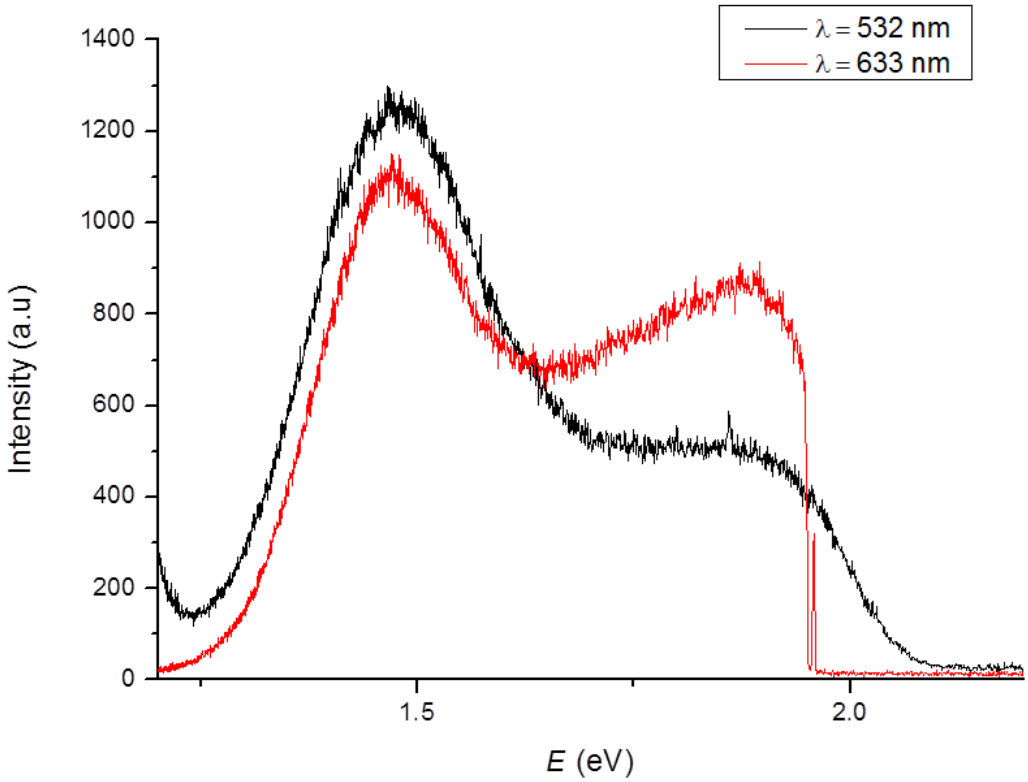

Figure 5.9: The effect of laser excitation wavelength on the Mn-related PL emission with $x = 12$ %, $P = 100$ W/cm^2 and $T = 300$ K.

It is also worth noting here the effect of the laser excitation wavelength on the Mn-related PL emission. The Mn-related emission is more prominent when excited resonantly (i.e. excitation energy close to that of the PL peak emission) at $\lambda = 633$ nm ($\sim$ 1.96 eV) than at 532 nm ($\sim$ 2.33 eV). Figure 5.9 shows the effect of laser excitation wavelength on the Mn-related PL emission. Here the measurements were taken on the same spot of the sample. The measurement using 633 nm excitation was taken first followed by the measurement using 532 nm excitation. This was also done in reverse with the 532 nm excitation measurement taken first

and the same effect was observed. When excited at 633 nm, an edge filter is used to cut the laser light to avoid damaging the detector. This filter blocks all light with $\lambda > 1.96$ eV and thus the PL signal drops to zero above this energy. As can be seen in Figure 5.9, the intensity starts to rise again at ~ 1.2 eV when using the 532 nm laser. This signal arises from the 2nd harmonic of the 532 nm laser at 1064 nm (1.17 eV).

Previous studies of Mn-doped II-VI systems do not report any quenching of the Mn-related band with time or under continuous illumination [8, 35]. On the other hand, in these previous studies the dots tend to contain a smaller Mn-concentration. Also, as mentioned previously, in the II-VI systems the Mn-related emission is at lower energies than the QD emission, thus creating a more favourable energy state for the carriers. This highlights a significant difference between our QDs and those reported in previous studies.

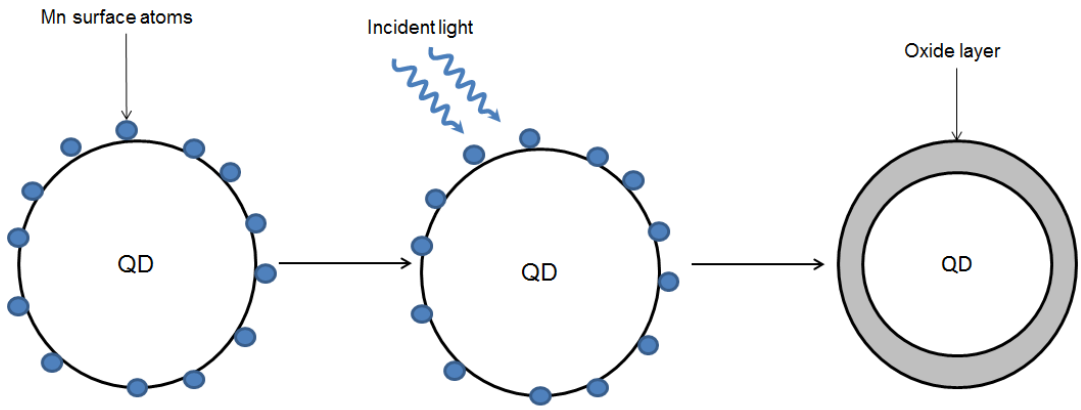

Figure 5.10: Cartoon showing the photo-oxidation process in Mn-doped PbS QDs.

These observations give evidence that a photo-oxidation process occurs in Mn-doped PbS QDs. We know from previous studies [8] and EPR results that Mn-atoms tend to migrate to the surface of the nanocrystals. We would not expect to see any emission form Mn-atoms in the core of the nanocrystal as they form a stable (PbMn)S alloy. Thus we can attribute the band centred at 1.9 eV to Mn surface atoms. As the photo-oxidation process takes place, these surface atoms form an oxide layer, from which we would not expect to see any PL emission. Thus we observe a quenching of the Mn-related emission over time as this oxide layer forms and the number of Mn surface atoms that contribute to the Mn emission are reduced. Figure 5.10 shows a cartoon of the photo-oxidation process and the

formation of an oxide layer. The photo-oxidation can reduce the effective size and number of surface defects leading to a subsequent blue-shift in the QD PL peak energy and an increase in the PL intensity, respectively. The presence of an oxide layer can also increase the height of the QD confinement potential thus contributing to the blue-shift of the PL emission.

To protect the Mn-doped QDs from oxidation, samples are stored in the dark in an N_2 environment. Despite these precautions, there may still be small amount of oxygen present in the environment which can produce small PL changes over time. These changes are mainly seen as a decrease of the Mn-related PL emission.

5.2 Photoinduced Raman Peaks

Evidence of photo-oxidation in $Pb_{1-x}Mn_xS$ nanoparticles have prompted further studies. By looking at the Raman spectra of the nanoparticles, and how these spectra change when exposed to continuous laser irradiation, could help to confirm that a photo-oxidation process is taking place.

As for the PL experiments, the nanoparticles were drop-cast on a glass substrate and exposed to laser light for a time $t_L = 30 - 125$ min. All measurements of the Raman spectra were taken with the corresponding PL spectra so the two could be compared directly. In all the experiments, the Raman spectra were measured first, followed by a measurement of the PL spectra. The longer integration times needed to obtain Raman spectra due to the low intensity of the scattered laser light (5 minutes in these experiments) means there is a significant temporal gap between the two measurements. Laser excitation wavelength of $\lambda = 633$ nm and power densities of $P = 100$ W/cm^2 were used in all experiments.

Figure 5.11 shows the Raman spectra and corresponding PL spectra for undoped PbS nanoparticles over 35 minutes of continuous illumination. Prominent Raman peaks appear after less than 10 minutes continuous irradiation. Two successive measurements were taken after 20 and 30 minutes with no further changes to the Raman spectra being observed. The most prominent peak highlighted in the figure is the peak at 203 cm^{-1}, which is close to the peak in bulk PbS at 209 cm^{-1} corresponding to longitudinal optical (LO) phonons [92] and similar to

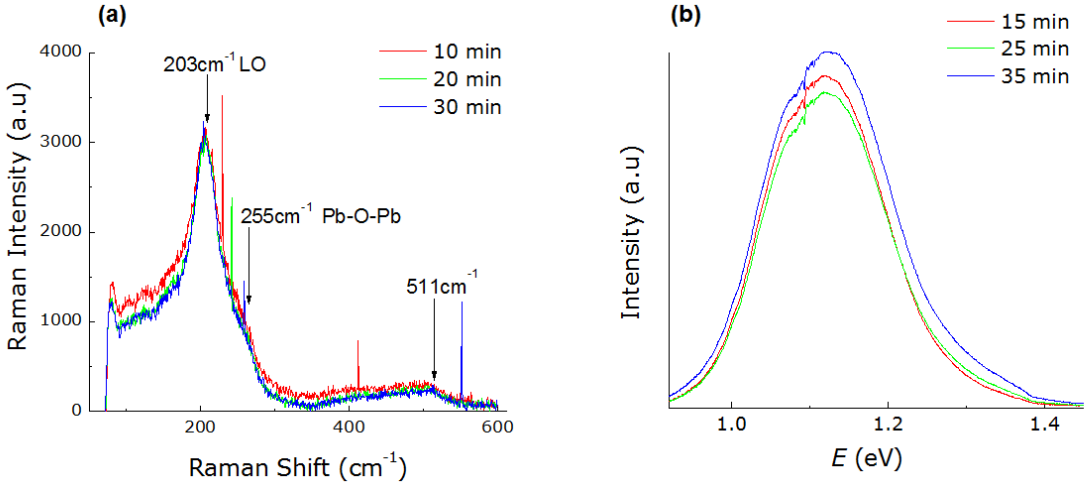

Figure 5.11: Raman spectra for PbS nanoparticles over 30 min continuous illumination (a) and corresponding PL spectra (b) ($\lambda = 633$ nm, $P = 100$ W/cm^2 and $T = 300$ K).

those previously reported for PbS nanoparticles (206 cm^{-1} [93]). Here the different frequency of the Raman peak compared to that of the bulk material is attributed to quantum confinement [94]. This peak has a reproducible shoulder at 255 cm^{-1}. The closest peak related to this in a bulk system corresponds to the Pb-O-Pb bond at 264 cm^{-1} [92]. In previous reports of PbS nanoparticles, the Raman peaks associated with these bonds are observed at a lower frequency of $\sim$ 270 cm^{-1} [87]. An additional weak feature is also observed at 511 cm^{-1}. This is not associated to any peak in bulk PbS and has not been reported in PbS nanoparticles. Although this peak is common in all nanoparticles, it is not always reproducible and could be a contribution from impurities.

Figure 5.12 shows the Raman spectra (a) and corresponding PL spectra (b) for $Pb_{1-x}Mn_xS$ nanoparticles with $x = 3$ % over 85 minutes of continuous irradiation. The figure shows the appearance of similar peaks to the PbS sample. However, no Raman peaks appear until after 65 minutes. The peak corresponding to the LO phonons has shifted to 207 cm^{-1}, higher than that of undoped PbS nanoparticles. The peak corresponding to the Pb-O-Pb bond has shifted by $\sim$ 2 cm^{-1} to 257 cm^{-1} whilst the unidentified peak at 511 cm^{-1} for PbS nanoparticles cannot be seen. The corresponding PL spectra show that the Raman peaks do not appear until the PL intensity enhancement saturates (see Figure 5.12c). There is also the appearance of a shoulder in the PL spectra at $\sim$ 1.6 eV after 65 minutes.

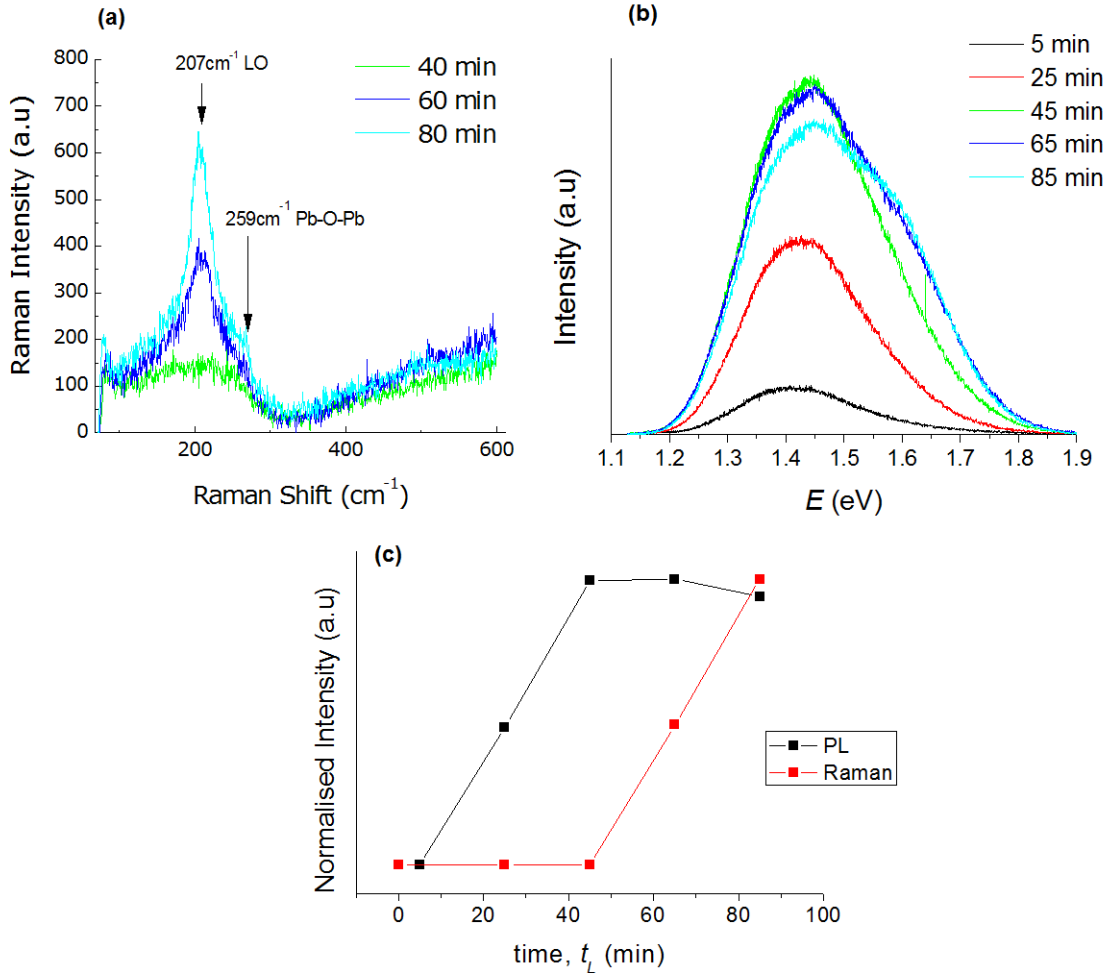

Figure 5.12: Raman spectra for $Pb_{1-x}Mn_xS$ nanoparticles ($x = 3$ %) over 85 min continuous illumination (a). Corresponding PL spectra (b). Normalised Raman and PL intensity versus time, t_L, (c) ($\lambda = 633$ nm, $P = 100$ W/cm^2 and $T = 300$ K).

Figure 5.13 shows the Raman spectra (a) and corresponding PL spectra (b) for $Pb_{1-x}Mn_xS$ nanoparticles with $x = 5$ % over 125 minutes of continuous irradiation. For this sample, 80 minutes of continuous irradiation was required before the appearance of Raman peaks. Once again the figure shows the appearance of similar Raman peaks to the two previous examples. The LO phonon peak is now at 208 cm^{-1} and the Pb-O-Pb related peak is at 259 cm^{-1}. For this sample there is an unidentified feature at 500 cm^{-1}. As with the previous sample, the corresponding PL spectra show that the Raman peaks do not appear until the PL intensity enhancement saturates (see Figure 5.13c). Again the PL spectra show a shoulder similar to that of the previous sample at ~ 1.6 eV, which manifests itself after 85 minutes.

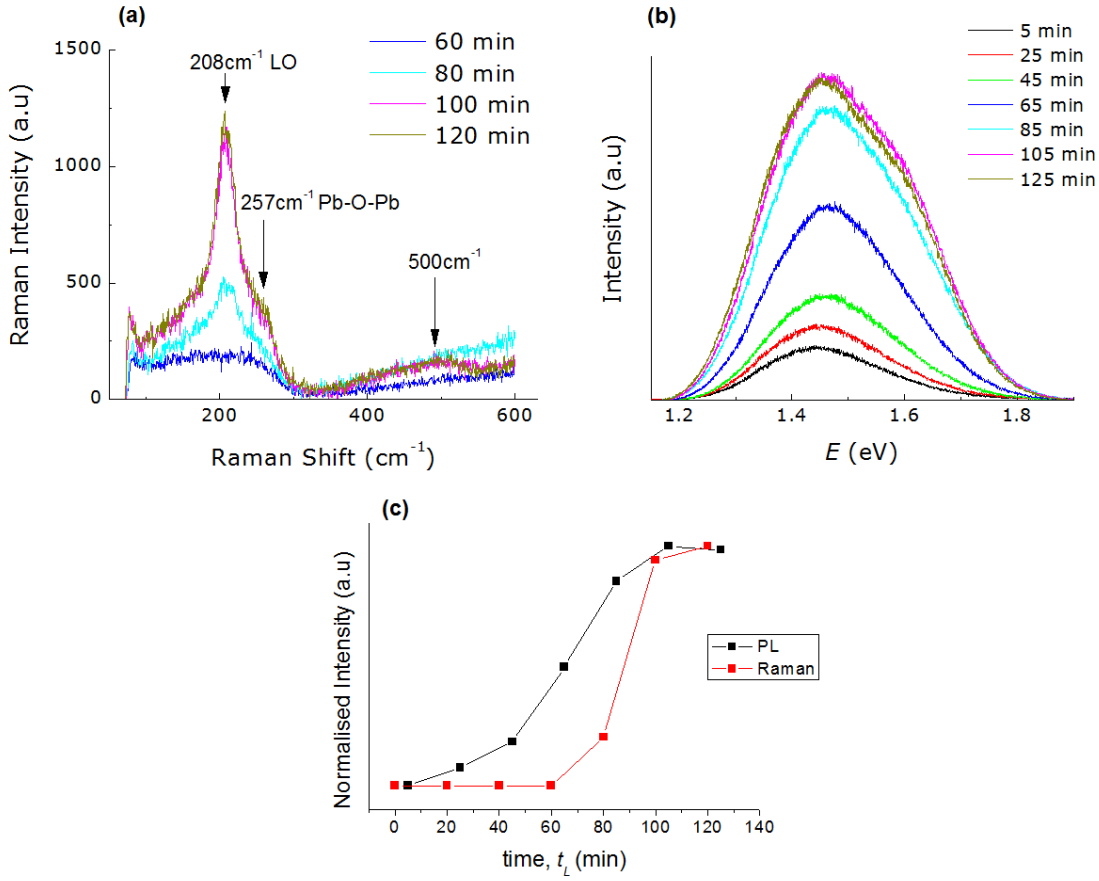

Figure 5.13: Raman spectra for $Pb_{1-x}Mn_xS$ ($x = 5$ %) nanoparticles over 125 min continuous illumination (a). Corresponding PL spectra (b). Normalised Raman and PL intensity versus time t_L, (c) ($\lambda = 633$ nm, $P = 100$ W/cm^2 and $T = 300$ K).

The appearance of Raman peaks over time can also be attributed to a photo-oxidation process. The Mn atoms and impurities on the surface of the nanoparticles will tend to absorb the laser light. Thus vibrational modes from the core of the nanocrystals cannot be seen. With continuous irradiation an oxide layer is formed on the surface of the nanoparticles (see Figure 5.10). This oxide layer will be comprised of both PbO and MnO, which have band gaps of 3.8 eV [95] and 2.3 eV [96], respectively. This layer is now transparent to laser light of wavelength of $\lambda = 633$ (1.95 eV), and the Raman peaks arising from bonding in the core of the nanoparticles can now be seen since the laser light is not absorbed on the surface. In the previous section we saw that undoped PbS nanoparticles did not undergo significant photo-oxidation. Therefore we would expect the Raman peaks appear to immediately or very quickly after illumination, in agreement with our observations.

The incorporation of Mn into $Pb_{1-x}Mn_xS$ nanoparticles prompts a systematic shift of the Raman peak, see Figures 5.14 (a) and (b). Figure 5.14 (a) shows how the LO phonon Raman peak depends on the Mn-content, x. With the formation of a (PbMn)S alloy, we would expect to see some changes in the bonding within the core of the nanocrystal, and thus changes in the Raman peaks. Although the incorporation with Mn effects the bonding, no peaks are observed relating to Mn, Mn oxidation products or Mn-S bonds.

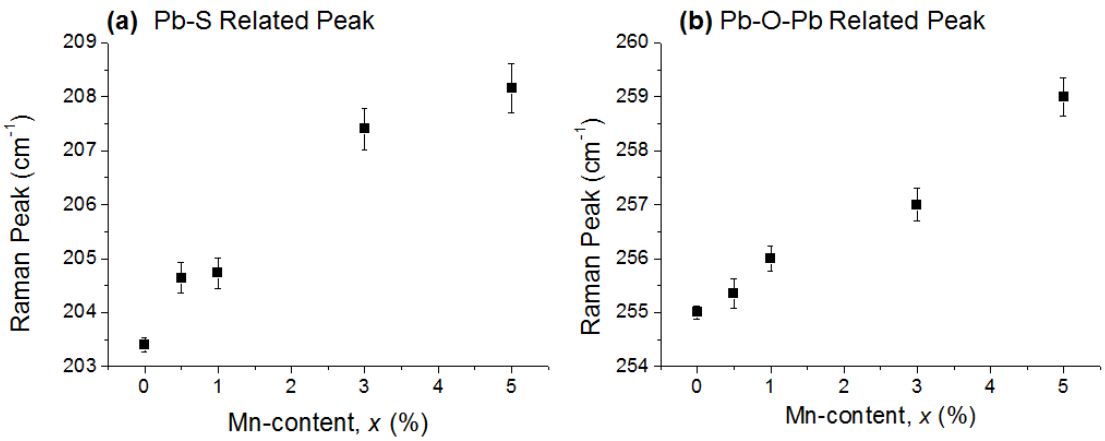

Figure 5.14: Graph showing how the Mn-content, x, effects the Raman peak related to the LO phonons (a) and Pb-O-Pb bond (b) in $Pb_{1-x}Mn_xS$ nanoparticles.

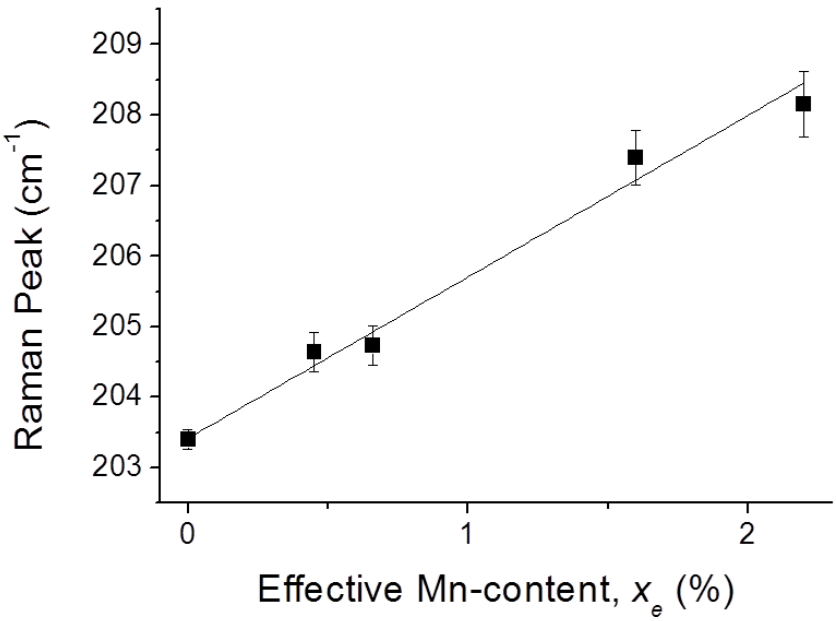

Figure 5.15: PbS LO optical phonon Raman peak versus the effective Mn-content. Solid line shows linear fit to the data.

Figure 5.15 shows how the LO phonon Raman peak depends on the effective Mn-content estimated from EDX and PL studies as discussed in chapter 4. A linear fit to the data indicates that the frequency of the LO Raman peak, R, can be described as

$$R(x) = R(0) + \alpha x \tag{5.1}$$

where $\alpha = 2.29$. For $x = 100$ % (i.e. MnS) this gives $R = 432$ cm^{-1}, which is close to the LO phonon mode reported for MnS (380 cm^{-1}) [97]. Broad PL emission spectra and the inability of EDX measurements to determine low concentrations of Mn suggest that Raman spectroscopy may, with further study, provide a more accurate method of estimating the effective Mn-content in $Pb_{1-x}Mn_xS$ QDs.

Chapter 6

Conclusions and Prospects for Future Work

The aim of this experimental study was to investigate how the magnetic and optical properties of colloidal PbS nanoparticles are affected by the controlled incorporation of Mn impurities. This work has provided a structural and chemical characterisation of Mn-doped PbS nanoparticles, and described how the photoluminescence, the temperature dependence of the photoluminescence and the magnetic properties are affected by the Mn-content. The effects of continuous laser irradiation on the nanoparticles were also studied and the subsequent photoinduced phenomena described.

We have demonstrated the controlled incorporation of Mn into PbS nanoparticles by EDX measurements. These measurements also showed that only a fraction of Mn used in the solution during synthesis is incorporated into the nanoparticles with effective doping levels of up to 8 %. We have shown by HRTEM and AFM measurements that the average size of the nanoparticles is $\sim$ 5 nm. These measurements also show that the size, shape and crystal structure of the nanoparticles are largely unaffected by the incorporation of Mn.

The effects of Mn on the room temperature PL properties were investigated and the observations can be summarised as follows. Mn incorporation has the effect of blue-shifting the PL peak emission, making the PL emission tunable in the

NIR wavelength range (850-1200 nm) and giving evidence for the formation of alloyed (PbMn)S nanoparticle. The PL intensity decreases by less than a factor of 10 going from $x = 0$ to 18 %, thus indicating a relatively low density of Mn-induced non-radiative recombination centres. Increasing Mn-content has the effect of broadening the optical linewidth, although a clear dependence of the broadening on x is not observed. The values of the Mn-concentration, Mn_{PL}, derived from the measured and calculated dependence of the PL peak energy, E_{QD}, on x are broadly in line with those derived by EDX, Mn_{EDX}, allowing us to estimate effective doping levels.

The PL properties were found to be strongly dependent on temperature. We observed a significant quenching of the PL intensity as the temperature increases. However, this property is not significantly affected by the Mn-content. The temperature dependence of the linewidth broadening was shown to be strongly dependent on the Mn-content, thus indicating a carrier-phonon interaction dependent on Mn. We observed a decrease of the temperature coefficient, $\alpha = dE_{QD}/dT$, with increasing Mn-content. This decrease is what we would expect for alloyed (PbMn)S nanoparticles, as it is positive for bulk PbS ($\alpha^{PbS} = +0.52$ meV/K) [12], but negative for MnS ($\alpha^{MnS} =$ - 2 meV/K) [14].

EPR and SQUID measurements have shown that the incorporation of Mn into PbS nanoparticles has the effect of imprinting them with paramagnetic properties. The EPR spectra reveal features characteristic of the hyperfine interaction of the d-electrons with the nuclear Mn spins. The asymmetric shape of the EPR lines indicates additional unresolved hyperfine splitting due to the contribution from Mn-ions on the surface and in the core of the nanoparticles, to be further investigated.

Continuous laser irradiation has the effect of blue-shifting the PL peak and significantly enhancing the PL intensity of Mn doped PbS nanoparticles. A clear dependence on the Mn-content was not observed. Photoinduced Raman peaks were also seen following continuous laser irradiation. These photoinduced phenomena suggested a photo-oxidation of the nanoparticles surface. Additional TEM studies of the nanoparticles after continuous laser irradiation could also give further evidence for the photo-oxidation of their surface.

A dependence of the frequency of the LO phonon Raman peak on the Mn-content was observed. As the frequency shifts linearly with the Mn-content, the frequency of the LO phonon mode could provide an accurate means of estimating the Mn-content in the nanocrystals. Further Raman an morphological studies studies are required to asses the validity of this method in the accurate determination of the dopant concentration in single nanocrystals.

In conclusion, this project has shown that the controlled incorporation of Mn atoms into PbS nanoparticles imprints them with interesting and unique optical and magnetic properties. Their tunable NIR PL emission and paramagnetic properties provide exciting prospects for their future exploitation in medical imaging as fluorescent biolabels and MRI contrast agents. Further studies into the effectiveness of the nanoparticles as MRI contract agents and luminescent biolabels, along with studies of their toxicity, will be required to show that these materials have a possible future in a clinical setting.

Bibliography

[1] A. P. Alivistos. *Science*, 271(5251):933–937, (1996).

[2] C. Burda, X. Chen, R. Narayanan, and M. A. El-Sayed. *Chem. Rev.*, 105:1025–1032, (2005).

[3] V. I. Klimov. *Nanocrystal Quantum Dots*. 2nd edition, (2004).

[4] A. Zrenner. *J. Chem. Phys.*, 7(3):359–366, (2000).

[5] Y. Wang, A. Suna, W. Mahler, and R. Kasowski. *J. Phys. Chem.*, 87(12):7315–7322, (1987).

[6] A. Santoni, G. Paolucci, G. Santoro, K. G. Prince, and N. E. Christensen. *J. Phys: Condens. Mater.*, 4:6759–6768, (1992).

[7] S. V. Kershaw, A. S. Susha, and A. L Rogach. *Chem. Soc. Rev.*, 42:3033–3087, (2013).

[8] N. Pradhan and A. Suna. *J. Phys. Chem. Lett.*, 2:2818–2822, (2011).

[9] D. J. Norris, N. Yao, F. T. Charnock, and T. A. Kennedy. *Nano Lett.*, 1:3–7, (2000).

[10] J. Cheon and J. H. Lee. *Acc. Chem. Res.*, 41, (2009).

[11] M. O. Manasreh. *Lead Chalcogenides Physics and Applications*. (2003).

[12] O. Madelung. *Semiconductor: Data Handbook*. Springer, 3rd edition, (2004).

[13] D. Isheim, J. Kaszpurenko, D. Yu, Z. Mao, D. N. Seidman, and I. Arslan. *J. Phy. Chem. C.*, 116:6595–6600, (2012).

[14] S. Mochizuki and N. Takayama. *J. Phys: Condens. Mater.*, 3:2729, (1991).

[15] G. Hodes. *Chemical Solution Deposition Of Semiconductor Films.* Marcel Dekker Inc., (2003).

[16] C Kittel. *Introduction to Solid State Physics.* Springer, 8th edition, (2005).

[17] C. Delerue and M. Lanno. *Nanostructures: Theory and Modelling.* Springer, (2004).

[18] A. I. Ekimov and A. A. Onuschenko. *Sov. Phys. Semicond.*, 16:775–780, (1982).

[19] D. J. Norris. *Semiconductor and Metal Nanocrystals: Synthesis and Electronic and Optical Properties.* (2004).

[20] J. L. Marin, R. Riera, and S. A. Cruz. *J. Phys: Condens. Matte.r*, 10(6):1349–1361, (1998).

[21] L. Brus. *J. Phys. Chem.*, 90(12):2555–2560, (1986).

[22] S. N. Jun, E. J. Jang, J. J. Park, and J. M. Kim. *Langmuir*, 22:2407–2411, (2006).

[23] C. P. Collier, T. Vossmyer, and J. R. Heath. *Annu. Rev. Phys. Chem.*, 49:371–404, (1998).

[24] P. Alivisatos and Y. Yin. *Nature*, 437:29–35, (2005).

[25] C. J. Lin, T. Liedl, R. A. Sperling, M. T. Frenandez-Aruelles, J. M. Costa-Frenandez, R. Pereiro, A. San-Medel, Chang W. H., and W. J. Parak. *J. Mater. Chem.*, 17:1343–1346, (2007).

[26] M. T. Harrison, S. V. Kershaw, M. G. Burt, A. L. Rogach, A. Kornowski, A. Eychmuller, and H. Weller. *J. Appl. Chem.*, 72:295–307, (2000).

[27] J. Tang and E. H. Sargent. *Adv. Mater.*, 23:12–29, (2011).

[28] A. Pourret, P. Guyot-Sionnest, and J. W. Elam. *Adv. Mater.*, 21:232–235, (2011).

[29] C. Blanco-Andujar, L. D. Tung, and N. T. K. Thanh. *Rep. Prog. Chem.*, 106:553–568, (2010).

[30] M. N. Nordin, J. Li, S. K. Clowes, and R. J. Curry. *Nanotec.*, 23(275701), (2012).

[31] M. S. Gaponenko, A. A. Lutich, N. A. Tolstik, A. A. Onushcenko, A. A. Malyarecih, E. P. Petrov, and K. V. Yumashev. *Phys. Rev. B.*, 82(125320), (2010).

[32] L. Turyanska, J. H. Blokland, U. Elfurawi, O. Makarovsky, C. M. Christianen, and A. Patané. *Phys. Rev. B.*, 89(193302), (2010).

[33] B. Ullrich, J. S. Wang, and G. J. Brown. *AIP Advances*, 2(042132), (2012).

[34] B. Ullrich and J. S. Wang. *App. Phys. Lett.*, 102(071905), (2013).

[35] S. C. Erwin, L. Zu, M. I. Haftell, A. L. Efros, T. A. Kennedy, and D. J. Norris. *Nature*, 437(7):91–94, (2005).

[36] J. D. Bryan and D. R. Gamelin. *Prog. Inorg. Chem.*, 54:47–126, (2005).

[37] H. Bednarski, J. Cisowski, and J. C. Portal. *J. Cryst. Growth*, 184(996-999), (1998).

[38] R. S. Silva, P. C. Morais, H. S. L. Sullasi, F. Qu, W. E. F. Aytab, and N. O. Dantas. *J. Alloys Compd.*, 483:204–206, (2009).

[39] N. O. Dantas, F. Pelegrini, M. A. Novak, P. C. Morais, G. E. Marques, and R. S. Silva. *J. Appl. Phys. III*, 111(064311), (2012).

[40] G. Long, B. Barman, S. Delikanli, Y. T. Tsaim, P. Zhang, and A. Petrou. *Appl. Phys. Lett.*, 101(062410), (2012).

[41] L. Vegard. *Zeithschrift Fur Physik*, 5:17–19, (1921).

[42] G. A. Wagneieres, W. M. Star, and B. C. Wilson. *Photochem. Photobiol.*, 68:603–632, (1998).

[43] X. Michalet, F. F. Pinaud, L. A. Bentolia, J. M. Tsay, S. Doose, J. J. Li, G. Sundaresan, A. M. Qu, S. S. Gambhir, and S. Weiss. *Science*, 307(5709), (2005).

[44] Y. Y. Huang, M. Hamblin, and A. C. H. Chen. *SPIE Newsroom*, (2009).

[45] M. A. Brown and R. C. Semelka. *MRI: Basic Principles and Applications.* 4th edition, (2011).

[46] Q. L. Voung, S. V. Doorslaer, J. L. Bridot, C. Argante, G. Alejanfro, R. Hermanm, S. Dish, C. Mattea, S. Stapf, and Y. Gossuin. *Pharm. Res.*, 29:1161–1179, (2011).

[47] J. Gao. *Acc. Chem. Res.*, 42(8):1097–1107, (2009).

[48] C. Rmenapp, B. Gleich, and A. Haase. *Pharm. Res.*, 29:1161–1179, (2011).

[49] K. T. Young, W. C. Law, R. Hu, A. Ling, L. Liwei, and M. T. Swiharte. *Chem. Soc. Rev.*, 42:1236–1240, (2013).

[50] L. Turyanska, T. D. Bradshaw, J. Sharpe, M. Li, S. Mann, N. R. Thomas, and A. Patané. *Small*, 5(15):1738–1742, (2009).

[51] R. Hardman. *Environ. Health Perspect.*, 114(2):165–170, (2005).

[52] L. Levina, W. Sukhovatkin, S. Musikhin, S. Cauchi, R. Nisman, D. P. Bazett-Jones, and E. H Sargen. *Adv. Mater.*, 17:1854–1859, (2005).

[53] L. Turyanska, M. Henini, B. Hennequin, N. R. Thomas, and A. Patané. *Appl. Phys. Lett.*, 90(101913), (2007).

[54] M. Fox. *Optical Properties of Solids.* Oxford University Press, (2004).

[55] A. B. Kira and S. W. Koch. *Semiconductor Quantum Optics.* Cambridge University Press, (2011).

[56] A. L. Efros, A. Karchenko, and M. Rosen. *Solid State Commun.*, 93(4):281–284, (1995).

[57] S. Baranovskii, R. Eichmann, and P. Thomas. *Phys. Rev. B.*, 58(19):13081–13087, (1998).

[58] C. V. Raman. *Nature*, 121:619–625, (1928).

[59] J. A. Weil and J. R. Bolton. *Electron Paramagnetic Resonance Spectroscopy: Elementary Theory and Applications.* Wiley-Interscience, 2nd edition, (2007).

[60] N. O. Dantos, A. Damigo, Q. Fanyao, R. S. Silva, P. P. C. Sartoratto, and K. L. Miranda. *J. Non-Cryst. Solids*, 354:4727–4729, (2008).

[61] S. T. Ochsenbein and D. R. Gamelin. *Nat. Nanotechnol.*, 6:112–115, (2010).

[62] R. C. Jaklevic, J. Lambe, A. H. Silver, and J. E. Mercereau. *Phys. Rev. Lett.*, 12(7):159–160, (1964).

[63] B. D. Josephson. *Phys. Lett.*, 1:251–255, (1962).

[64] K. Tsuji, J. Injuk, and R. V. Grieken. *X-Ray Spectroscopy: Recent Technological Advances.* Wiley, 2004.

[65] G. Binnig and C. F. Quate. *Phys. Rev. Lett.*, 56(9):930–933, (1986).

[66] G. Binnig and Roher H. *Appl. Phys. Lett.*, 40:178–180, (1981).

[67] J. B. Pethica and W. C. Oliver. *Physica Scripta.*, 19:61–66, (1987).

[68] F. J. Giessibl. *Rev. Mod. Phys*, 75:949–983, (2003).

[69] S. Morita, R. Wiesendanger, and E. Meyer. *Non-contact atomic force microscopy.* Wiley, (2004).

[70] R. Egerton. *Physical principles of electron microscopy.* Springer, (2005).

[71] D. B. Williams and C. B. Carter. *Transmission Electron Microscopy: A Textbook for Materials Science : Basics, Diffraction, Imaging, Spectrometry.* Spinger, (1996).

[72] D. J. Smith. *Rep. Prog. Phys.*, 60:1513–1580, (1997).

[73] M. Flores-Acosta, M. Sotelo-Lermac, H. Arizpe-Cháves, F. F. Castillón-Barrazam, and Ramírez-Bon R. *Solid State Commun.*, 128:407 – 411, (2003).

[74] B. Hennequin, L. Turyanska, T. Ben, M. Beltran, S. I. Molina, S. Mann, M. Li, A. Patané, and N. R. Thomas. *Adv. Mater.*, 20:3592–3598, (2009).

[75] A. Louie. *Chem. Rev.*, 110:3146–3150, (2010).

[76] S. Sanguinetti, E. Poliani, M. Bonfanti, M. Guzzi, M. Grilli, E.and Gurioli, and N. Koguchi. *Phys. Rev. B.*, 730(125342), (2006).

[77] V. M. Fomin, V. N. Galdilin, J. T. Devreese, E. P. Pokatilov, Balabn S. N., and Klimin S. N. *Phys. Rev. B.*, 57:2415–2419, (1998).

[78] M. Balkanski and R. F. Wallis. *Semiconductor Physics and Applications.* Oxford University Press, (2000).

[79] A. Olkhovets, R. C. Hsu, A. Lipovskii, and F. W. Wise. *Phys. Rev.*, 81(16):3539–3542, (1998).

[80] B. Ullrich, J. S. Wang, and G. J. Brown. *Appl. Phys. Lett.*, 99(081901), (2011).

[81] R. V. Kamat and N. M. Dimitrijevic. *J. Phys. Chem*, 93:2873–2875, (1988).

[82] R. S. Silva, P. C. Morais, F. Qu, A. M. Alcalde, N. O. Dantos, and H. S. L. Sullasi. *Appl. Phys. Lett.*, 90(253114), (2007).

[83] J. W. Stoudam, J. Shan, and F. C. J. van Veggel. *J. Phys. Chem. C*, 111:1086, (2007).

[84] W. van Sark, P. Frederix, D. J. Heuvel, Gerritsen H. C., A. A. Joost, N. J. van Lingen, C. Donegea, and A. Meijerink. *J. Phys. Chem. B*, 105:8281–8284, (2001).

[85] M. Jones, J. Nedeljkovic, R. J. Ellingson, A. J. Nozik, and G. Rimbles. *J. Phys. Chem. B*, 107:11346–11352, (2003).

[86] T. Zhang, H. Zhao, D. Riabinina, M. Chaker, and Ma. D. *J. Phys. Chem. C*, 114:10153–10159, (2010).

[87] J. L. Blackburn, Luther M. J. Chappell, H., A. J. Nozik, and Johnson J. C. *J. Phys. Chem. Lett.*, 2:599–603, (2011).

[88] C. K. Lui, Y. K. Kwon, and J. Heo. *Appl. Phys. Lett.*, 90(241111), (2007).

[89] S. R. C. Cordero, R. A. Estabrook, G. F. Strouse, and S. K. Buratto. *J. Phys. Chem. B*, 140:1237–1240, (2000).

[90] A. Y. W. Nazzal, L. Qu, W. Yu, Y. Wang, X. Peng, and M. Xiao. *J. Phys. Chem. B*, 108:5507–5511, (2004).

[91] T. M. Uematsu and Y. Yamaguci. *J. Phys. Chem. B*, 109:8613–8615, (2005).

[92] Y. Battonneau, C. Brémard, J. Laureyns, and J. C. Merlin. *J. Raman Spectrosc.*, 31:1113–1119, (2000).

[93] A. V. Baranova, K. V. Bogdanova, E. V. Ushakovaa, A. V. Cherevkova, A. V. Fedorova, and S. Tscharntkeb. *Condens. Matter. Spectrosc.*, 109:301–305, (2010).

[94] T. D. Krauss and F. W. Wise. *Phys. Rev. B.*, 55(15):9860–9862, (1996).

[95] D. O. Scanlon, A. B. Keoe, G. W. Watson, M. O. Jones, W. I. F. David, D. J. Payne, R. G. Egdell, P. P. Edwards, and A. Walsh. *Phys. Rev. Lett.*, 107(246402), (2011).

[96] F. Tran and R. Blaha. *Phys. Rev. Lett.*, 102(226401), (2009).

[97] L. David, X. Tang, G. Beamson, D. Wolverson, K. A. Prior, and B. C. Cavnett. *phys. stat. sol. (b)*, 241(3):471–474, (2044).